Journal of Computational Physics 229 (2010) 3065–3090

Contents lists available at ScienceDirect

Journal of Computational Physics

journal homepage: www.elsevier.com/locate/jcp

A unified approach to energy conservation and potential vorticity dynamics for arbitrarily-structured C-grids

T.D. Ringler [a,*], J. Thuburn [b], J.B. Klemp [c], W.C. Skamarock [c]

[a] Theoretical Division, Los Alamos National Laboratory, Los Alamos, NM 87545, USA
[b] Mathematics Research Institute, School of Engineering, Computing and Mathematics, University of Exeter, Exeter EX4 4QF, UK
[c] National Center for Atmospheric Research, Boulder, CO 80307, USA

ARTICLE INFO

Article history:
Received 29 July 2009
Received in revised form 29 October 2009
Accepted 7 December 2009
Available online 28 December 2009

Keywords:
C-grid
Voronoi diagram
Potential vorticity
Shallow-water equations

ABSTRACT

A numerical scheme applicable to arbitrarily-structured C-grids is presented for the nonlinear shallow-water equations. By discretizing the vector-invariant form of the momentum equation, the relationship between the nonlinear Coriolis force and the potential vorticity flux can be used to guarantee that mass, velocity and potential vorticity evolve in a consistent and compatible manner. Underpinning the consistency and compatibility of the discrete system is the construction of an auxiliary thickness equation that is staggered from the primary thickness equation and collocated with the vorticity field. The numerical scheme also exhibits conservation of total energy to within time-truncation error. Simulations of the standard shallow-water test cases confirm the analysis and show convergence rates between 1st- and 2nd-order accuracy when discretizing the system with quasi-uniform spherical Voronoi diagrams. The numerical method is applicable to a wide class of meshes, including latitude–longitude grids, Voronoi diagrams, Delaunay triangulations and conformally-mapped cubed-sphere meshes.

Published by Elsevier Inc.

1. Introduction

In a previous and related effort, Thuburn et al. [35], hereafter T09, consider the formulation of a discrete method for robust simulation of geostrophic adjustment. When the geostrophic adjustment problem is considered with a constant Coriolis parameter, the continuous linear system supports a stationary mode in geostrophic balance that is characterized by purely rotational flow; divergence is everywhere identical to zero for all time and the time tendency of vorticity is also zero for all time. In the limit of geostrophic balance, the steady-state flow is along lines of constant pressure with an exact cross-flow balance between the horizontal pressure gradient force and the Coriolis force.

The discrete method considered in T09 is a finite-volume approach based on a C-grid staggering. This approach retains prognostic equations for mass at the center of finite-volume cells and for the normal component of velocity at the faces (or edges in 2D) of finite-volume cells. While C-grid methods lead to an excellent representation of gravity waves in relation to other finite-volume grid staggerings [4], the method's ability to reproduce geostrophic balance is sometimes problematic [20]. The root cause of this problem is in the discrete formulation of the Coriolis force; the Coriolis force is proportional to the tangential component of velocity, which is not known. Since the tangential velocities are not known, these velocities must be reconstructed based on neighboring values of normal velocity. The primary result of T09 is the derivation of a robust method for the reconstruction of the tangential velocities on arbitrarily-structured C-grids such that the discrete system allows exact geostrophic balance to be maintained when appropriate.

* Corresponding author.
E-mail addresses: ringler@lanl.gov (T.D. Ringler), j.thuburn@ex.ac.uk (J. Thuburn), klemp@ucar.edu (J.B. Klemp), skamaroc@ucar.edu (W.C. Skamarock).

0021-9991/$ - see front matter Published by Elsevier Inc.
doi:10.1016/j.jcp.2009.12.007

T09 limited the scope of analysis to the linearized shallow-water equations. The primary purpose of this present effort is to extend the previous analysis to the nonlinear shallow-water equations with focus on the analysis of potential vorticity dynamics and system energetics within the discrete system. Even though the analysis of T09 is carried out for the linearized shallow-water equations with a constant Coriolis parameter, their results are essential for the extension to the full nonlinear shallow-water equations solved on the sphere.

With the growing interest in the use of unstructured meshes for the simulation of ocean and atmosphere flows, a significant amount of effort has been devoted to the treatment of the Coriolis force in C-grid methods. While the reconstruction of the tangential velocity required for computing acceleration due to the Coriolis force is straightforward on square meshes, the task becomes significantly more difficult on other meshes, such as Voronoi diagrams or Delaunay triangulations. While in the continuous system the Coriolis force is orthogonal to the velocity vector and, thus, energetically-neutral, this property is not trivial to satisfy for a C-grid staggering on arbitrarily-structured meshes. Since the Coriolis force can serve as an infinite source of kinetic energy in discrete systems where it is not energetically-neutral, efforts in reconstructing the discrete Coriolis force have sometimes focused exclusively on system energetics (e.g. [30,12,15]). Significantly fewer efforts have recognized that the Coriolis force is not only central to the energetics of the discrete system, but also plays a fundamental role in the discrete vorticity budget (e.g. [23,6]). While conservation of energy and absolute vorticity are critically important aspects of discrete models that are intended to simulate geophysical flows, these properties are not sufficient for the robust simulation of geophysical flows. The critical aspect of the discrete system that has to be included is that of potential vorticity dynamics, as was address by [26,2]. The primary purpose of this contribution is to derive a discrete method on arbitrarily-structured C-grids that allows for the conservation of total energy *and* a robust simulation of potential vorticity dynamics. As shown below, a single term in the momentum equation, the nonlinear Coriolis force, plays a central role in both the energy and potential vorticity dynamics. As a result, energy and potential vorticity cannot be adequately treated in isolation, but require a unified approach.

The results of T09 are particularly relevant to the construction of the discrete potential vorticity (PV) equation. Potential vorticity has proven to be a key quantity in the theoretical and observational interpretation of atmosphere and ocean dynamics (e.g. [7,18]). As discussed in Hoskins et al. [14], the broad utility of PV stems both from its ability to inform local processes by acting as a Lagrangian tracer and from its ability to inform large-scale, balance-dominated processes through the principle of invertibility. Given the fundamental importance of PV in geophysical flows, numerical models are sometimes constructed to faithfully represent some aspects of the PV dynamics within the discrete system (e.g. [2,26,33,16]). We carry forward that idea here, but have to overcome two significant hurdles to be successful.

The first hurdle is one of *compatibility* with the momentum equation. In a C-grid method, the discrete PV equation is obtained by applying the discrete curl operator to the velocity equation, then combining that result with a discrete equation for layer thickness. Compatibility with the momentum equation is the ability to derive a flux-form expression of the PV equation that is a direct analog of its continuous counterpart in the sense that the tendency of thickness-weighted PV is due solely to one term and that term is the divergence of a PV flux. Compatibility in the sense defined here is sufficient to guarantee local and global *conservation* since the sole forcing term in the discrete PV equation is the divergence of a flux.

The second hurdle is one of *consistency* with the Lagrangian behavior of PV. In the frictionless and adiabatic limit, PV evolves as

$$\frac{Dq}{Dt} = 0, \tag{1}$$

where q is PV and D/Dt is the material derivative. For the numerical scheme to be considered consistent with respect to the Lagrangian behavior of PV, we require the discrete system to possess an analog to (1) in the sense that the discrete PV field evolves with the same material derivative as the underlying continuity equation from which the PV is derived.

In a finite-volume formulation, a consistent representation of the PV Lagrangian property requires that the flux-form PV equation be consistent with an underlying flux-form thickness equation such that if $q(\mathbf{x}, t)$ is uniform (i.e. independent of $\mathbf{x}$) at some time t, then $q(\mathbf{x}, t)$ is uniform for all time. We consider consistency with the Lagrangian properties of PV to include the preservation of a constant PV field for all time. It is important to note that within a finite-volume formulation, compatibility with the momentum equation is a necessary prerequisite for consistency with the Lagrangian property of PV.

Finite-volume methods designed for simulation of geophysical flows are often constructed to mimic integral constraints found in the continuous system, such as conservation of thickness-weighted PV in the shallow-water system that follows from compatibility. However, conservation of PV in the discrete system is not sufficient to guarantee that the discrete system mimics the Lagrangian property of PV defined in (1). In particular, conserving PV in the shallow-water system does not guarantee consistency. The lack of control that conservation exerts on the Lagrangian property of PV is frequently overlooked, e.g. [6], and results in less robust simulations.

The aim of this contribution is to construct the discrete principles of PV compatibility and consistency, along with the principle of total energy conservation, within the very general framework of arbitrarily-structured meshes. These discrete principles have been demonstrated before, but only for regular grids, such as square meshes (e.g. [26,2]). The results produced below hold for a broad class of meshes that utilize the C-grid staggering, including arbitrary Voronoi diagrams [11], arbitrary Delaunay triangulations [6], stretched-poles grids [29] and conformally-mapped cubed-sphere meshes [1]. The requirement for the method derived below to hold is that the mesh be locally orthogonal in the sense that the edges

that define mass cells and the edges that define vorticity cells are perpendicular at their intersection. The findings of Sadourny [26] on a square mesh are recovered as a special case of this general method.

While the method holds for a broad class of meshes, the example simulations used to confirm the analytic results are constructed using the Voronoi diagram and Delaunay triangulations. Voronoi diagrams and Delaunay triangulation are deeply connected. A specification of either uniquely determines the other. For this reason, the two meshes are often referred to as *duals*. The strong relationship proves extremely useful when developing staggered-grid methods that require extensive use of both a prime mesh and a dual mesh. In addition, the Voronoi–Delaunay combination along with the C-grid staggering combine to form a discrete analog of the Helmoltz decomposition [21]. Thus, the vorticity and divergence fields contain equivalent information to the velocity field in the discrete system, as they do in the continuous system. This relationship proves useful when attempting to connect the evolution of velocity to the evolution of vorticity.

The paper is presented as follows: Section 2 discusses principles of PV dynamics and energy conservation within the context of the continuous system. Special attention in Section 2 is given to the relationship between the PV flux and the nonlinear Coriolis force. Section 3 develops the discrete system such that the principles of PV consistency, compatibility and conservation and total energy conservation hold. Section 4 presents numerical results intended primarily to confirm the analytical findings. Section 5 concludes with a discussion of possible extensions of the proposed method and the types of problems that become tractable using these techniques.

2. Governing equations

2.1. Nonlinear shallow-water equations

The nonlinear shallow-water equations can be expressed as

$$\frac{\partial h}{\partial t} + \nabla \cdot (h\mathbf{u}) = 0, \tag{2}$$

$$\frac{\partial \mathbf{u}}{\partial t} + (\mathbf{u} \cdot \nabla)\mathbf{u} + f\mathbf{k} \times \mathbf{u} = -g\nabla(h + b) + \mu\mathbf{k}, \tag{3}$$

where prognostic equations are written for the evolution of the fluid thickness, h, and the fluid vector velocity, $\mathbf{u}$. The unit vector, $\mathbf{k}$, points in the local vertical direction. We consider the velocity field to exist in $\mathbb{R}^3$ and the Lagrange multiplier, $\mu\mathbf{k}$, is formally included following [8] to constrain $\mathbf{u}$ to the $\mathbb{R}^2$ surface of the sphere. We assume throughout that $\mathbf{k} \cdot \mathbf{u} \equiv 0$. The three parameters in the system are gravity, g, Coriolis parameter, f, and bottom topography, b. The discretization of the nonlinear transport term in (3) is problematic when considering issues related to potential vorticity and energy conservation. An alternative is to transform (3) into what is commonly referred to as the "vector-invariant form" that is obtained by using the vector identity,

$$(\mathbf{u} \cdot \nabla)\mathbf{u} = (\nabla \times \mathbf{u}) \times \mathbf{u} + \nabla \frac{|\mathbf{u}|^2}{2}, \tag{4}$$

to replace the $(\mathbf{u} \cdot \nabla)\mathbf{u}$ term in (3) to obtain

$$\frac{\partial \mathbf{u}}{\partial t} + \eta\mathbf{k} \times \mathbf{u} = -g\nabla(h + b) - \nabla K, \tag{5}$$

where $\eta = \mathbf{k} \cdot \nabla \times \mathbf{u} + f$ is the absolute vorticity and $K = |\mathbf{u}|^2/2$ is the kinetic energy.[1]

In the shallow-water system the fluid PV is related to the absolute vorticity and thickness field as

$$q = \frac{\eta}{h}. \tag{6}$$

Using (6) we can rewrite (5) to produce

$$\frac{\partial \mathbf{u}}{\partial t} + q(h\mathbf{u}^\perp) = -g\nabla(h + b) - \nabla K, \tag{7}$$

where $\mathbf{u}^\perp = \mathbf{k} \times \mathbf{u}$. The term $q(h\mathbf{u}^\perp)$ is interpreted as the thickness flux, $h\mathbf{u}^\perp$, of PV in the direction perpendicular to the velocity $\mathbf{u}$. We refer to $q(h\mathbf{u}^\perp)$ as the nonlinear Coriolis force since it contains the quasi-linear Coriolis force $f\mathbf{u}^\perp$ *and* the rotational part of the nonlinear transport term $(\mathbf{u} \cdot \nabla)\mathbf{u}$. Note that due to the inclusion of the rotational part of the nonlinear transport term, the "nonlinear Coriolis force" is no longer entirely an artifact of posing the equations in a rotating coordinate system. The benefits of using (7) as the basis for the discrete model are discussed below.

[1] When moving from (3) to (5) using (4), the Lagrange multiplier term in (3) is eliminated. This can be seen by expanding $(\nabla \times \mathbf{u}) \times \mathbf{u}$ in, say, spherical polar coordinates. In addition to recovering the $\eta\mathbf{k} \times \mathbf{u}$ in (5) we obtain an additional tendency term in the local vertical direction. The requirement that this term should exactly cancel the Lagrange multiplier term determines the value of μ. The remaining terms in the equation are then purely horizontal.

2.2. Vorticity and divergence formulation

Vorticity and divergence are *derived* quantities; both quantities are obtained through manipulation of the velocity equation. The vorticity and divergence equations can be obtained by taking $\mathbf{k}\cdot\nabla\times$ (7) and $\nabla\cdot$(7), respectively, to yield

$$\frac{\partial \eta}{\partial t} + \mathbf{k}\cdot\nabla\times\left[\eta\mathbf{u}^{\perp}\right] = 0, \tag{8}$$

$$\frac{\partial \delta}{\partial t} + \nabla\cdot\left[q h\mathbf{u}^{\perp}\right] = -g\nabla^2(h+b) - \nabla^2 K, \tag{9}$$

where $\delta = \nabla\cdot\mathbf{u}$ is the divergence and we have replaced $\partial(\mathbf{k}\cdot\nabla\times\mathbf{u})/\partial t$ by $\partial\eta/\partial t$ in (8) since $\partial f/\partial t = 0$. We can manipulate (8) into a more familiar form by noting that $\mathbf{k}\cdot\nabla\times[\eta\mathbf{u}^{\perp}] = \nabla\cdot[\eta\mathbf{u}]$ to obtain

$$\frac{\partial \eta}{\partial t} + \nabla\cdot[\eta\mathbf{u}] = 0. \tag{10}$$

Given the relationship between absolute vorticity and PV, we can rewrite (10) as

$$\frac{\partial}{\partial t}(hq) + \nabla\cdot[qh\mathbf{u}] = 0. \tag{11}$$

Note that (1) can be recovered by combining (2) and (11). By virtue of the Helmoltz Decomposition Theorem, e.g. [22], vorticity and divergence form a *complete* description of the underlying velocity vector; if one has access to the vorticity and divergence fields, then the velocity field is uniquely known (for a simple domain). Since the equation sets [(10), (9)] or [(11), (2), (9)] form a complete description of the underlying vector velocity field, either combination can be used as the basis for a numerical model,[2] with the former combination utilized in, for example, [24] and the latter combination utilized in, for example, [33]. The benefit of retaining hq as a prognostic equation is that the evolution of PV can be strongly controlled through the calculation of the flux divergence term $\nabla\cdot[\eta\mathbf{u}]$ via the use of advanced flux-transport algorithms (e.g. [38,32,17]). The ability to guarantee that the evolution of PV is, for example, monotone comes at the cost of having to invert elliptic equations at every time step and the possibility of having to satisfy additional boundary conditions. One purpose of this analysis is to exhibit a method that retains the vector velocity as a prognostic variable, yet also allows for the same level of control over the evolution of the PV field as retaining PV as the prognostic variable.

2.3. Relationship between the nonlinear Coriolis force and PV flux

The time tendency of the PV in (11) is due solely to the $\nabla\cdot[q\,h\mathbf{u}]$ term, i.e. to the divergence of the PV-weighted thickness flux. If we start at (11) and work backwards to trace the origins of the thickness-weighted PV flux term, our search ends at (7) with the $qh\mathbf{u}^{\perp}$ term. Stated explicitly we find

$$\frac{\partial}{\partial t}(hq) = -\nabla\cdot[q\,h\mathbf{u}] = -\mathbf{k}\cdot\nabla\times\left[q\,h\mathbf{u}^{\perp}\right]. \tag{12}$$

So, in fact, the PV-weighted thickness flux that is entirely responsible for the evolution of hq *is* the nonlinear Coriolis force in (7). While this relationship has long been exploited in numerical schemes, it might be fair to say that the relationship has not been discussed with the visibility it deserves. This relationship is often a key part of discretizations of the velocity equation (e.g. [2,26]); these works derive a discrete PV equation that is both consistent and conservative. The consistency is obtained by demonstrating that the discrete system can combine analogs of (2) and (11) to recover a discrete analog of (1). More recently, Lin and Rood [16] used the relationship between the nonlinear Coriolis force and PV flux while developing algorithms for solving the shallow-water equations on staggered grids. The discrete analysis below follows the lead of and builds from these previous works. We extend the line of research by demonstrating the ability to enforce certain constraints on the time evolution of PV, such as monotonicity, variance-diminishing behavior, variance preserving behavior, or energetically-neutral behavior through the proper discretization of $\mathbf{k}\cdot\nabla\times[qh\mathbf{u}^{\perp}]$ in (7).

2.4. Energy relations in the shallow-water system

In addition to an analysis of the potential vorticity dynamics of the discrete system, we also consider the energetic consistency of the discrete system. Since most of the degrees of freedom in the discrete system can be constrained through the principle of energy conservation, an abbreviated analysis of the energy relations in the shallow-water system is provided here in order to place the discrete derivation given below into context.

[2] The application of the curl and divergence operators increases by one the order of the partial differential equation. As a result, additional boundary conditions are required to close the system. In simple domains these extra boundary conditions are trivially satisfied. In more complicated domains, such as when fluid surfaces intersect topography, these boundary conditions can be cumbersome to satisfy in a discrete numerical model. See [19] for details.

The kinetic energy equation is derived by first multiplying (7) by $h\mathbf{u}$ to obtain

$$h\mathbf{u}\cdot\left[\frac{\partial \mathbf{u}}{\partial t}+q(h\mathbf{u}^{\perp})=-g\nabla(h+b)-\nabla K\right], \tag{13}$$

$$h\frac{\partial K}{\partial t}+h\mathbf{u}\cdot\nabla K=h\mathbf{u}\cdot[-g\nabla(h+b)], \tag{14}$$

where the fact that $\mathbf{u}\cdot\mathbf{u}^{\perp}=0$ has been used to eliminate the nonlinear Coriolis force. The kinetic energy equation is completed by multiplying (2) by K and adding the result to (14) to obtain

$$\frac{\partial (hK)}{\partial t}+\nabla\cdot(hK\mathbf{u})=h\mathbf{u}\cdot[-g\nabla(h+b)]. \tag{15}$$

Eq. (15) is the evolution equation for kinetic energy. The RHS of (15) represents a sink of kinetic energy as the fluid moves in the direction of increasing $(h+b)$. Eqs. (14) and (15) clearly show that K is a constant along particle trajectories when the source/sink term on the RHS is zero.

The potential energy equation is obtained by multiplying (2) by $g(h+b)$ to find

$$\frac{\partial}{\partial t}\left[gh\left(\frac{1}{2}h+b\right)\right]=-g(h+b)\nabla\cdot(h\mathbf{u}). \tag{16}$$

Eq. (16) is the potential energy equation where the RHS represents a sink of potential energy in regions where the thickness-flux divergence is positive. The total energy equation is determined by adding (15) and (16) to obtain

$$\frac{\partial E}{\partial t}+\nabla\cdot(hK\mathbf{u})=-\nabla\cdot[g(h+b)h\mathbf{u}], \tag{17}$$

where

$$E=hK+gh\left(\frac{1}{2}h+b\right) \tag{18}$$

is the total energy.

There are at least three aspects of the continuous energy equation that are beneficial to mimic in the discrete system. The first is that the nonlinear Coriolis force neither creates nor destroys energy. The second aspect is that the flux–divergence term $\nabla\cdot(hK\mathbf{u})$ in (17) is numerically preserved when combining the discrete forms of $K\times$ (2) and (13), implying that K is conserved under transport. And the third aspect is that source terms on the RHS of (15) and (16) combine to form a flux divergence term to ensure conservation of total energy. If these three aspects of the total energy budget can be mimicked in the discrete system, then we can be assured that the discrete model will not exhibit spurious growth or decay of energy over time.

3. Discrete system

3.1. Notation

The discrete system requires the definition of seven elements. These seven elements are composed of two types of *cells*, two types of *lines*, and three types of *points*. These elements are depicted in Fig. 1 and defined in Table 1. Let the space (either the plane or the surface the sphere) be tessellated by two meshes, a primal mesh composed of N_i cells and a dual mesh composed of N_v cells. Each corner of a primal mesh cell is uniquely associated with the "center" of a dual mesh cell and vice versa. The two types of cell objects are primal mesh cells P_i and dual mesh cells D_v. Let the center of any primal mesh cell, P_i, be denoted by $\mathbf{x}_i$ and the center of any the dual mesh cell, D_v, be denoted by $\mathbf{x}_v$. The boundary of a given primal mesh cell P_i is composed of the set of lines that connect the $\mathbf{x}_v$ locations of associated dual mesh cells D_v. Similarly, the boundary of a given dual mesh cell D_v is composed of the set of lines that connect the $\mathbf{x}_i$ locations of the associated primal mesh cells P_i.

As shown in Fig. 1, a line segment that connects two primal mesh cell centers is uniquely associated with a line segment that connects two dual mesh cell centers. For this analysis we assume that these two line segments cross and the point of intersection is labeled as $\mathbf{x}_e$. In addition, we assume that these two line segments are orthogonal as indicated in Fig. 1 (for a full treatment of the properties of the Voronoi diagram, including the property of orthogonality, see [5]). Each $\mathbf{x}_e$ is associated with two distances: d_e measures the distance between the primal mesh cells sharing $\mathbf{x}_e$ and l_e measures the distance between the dual mesh cells sharing $\mathbf{x}_e$.

Since the two line segments crossing at $\mathbf{x}_e$ are orthogonal, these line segments form a convenient local coordinate system for each edge. At each $\mathbf{x}_e$ location a unit vector $\mathbf{n}_e$ is defined to be parallel to the line connecting primal mesh cells. A second unit vector $\mathbf{t}_e$ is defined such that $\mathbf{t}_e=\mathbf{k}\times\mathbf{n}_e$.

In addition to these seven element types, we require the definition of *sets of elements*. In all, eight different types of sets are required and these are defined and explained in Table 2 and Fig. 2. The notation is always of the form of, for example, $i\in CE(e)$, where the LHS indicates the type of element to be gathered (cells) based on the RHS relation to another type of element (edges).

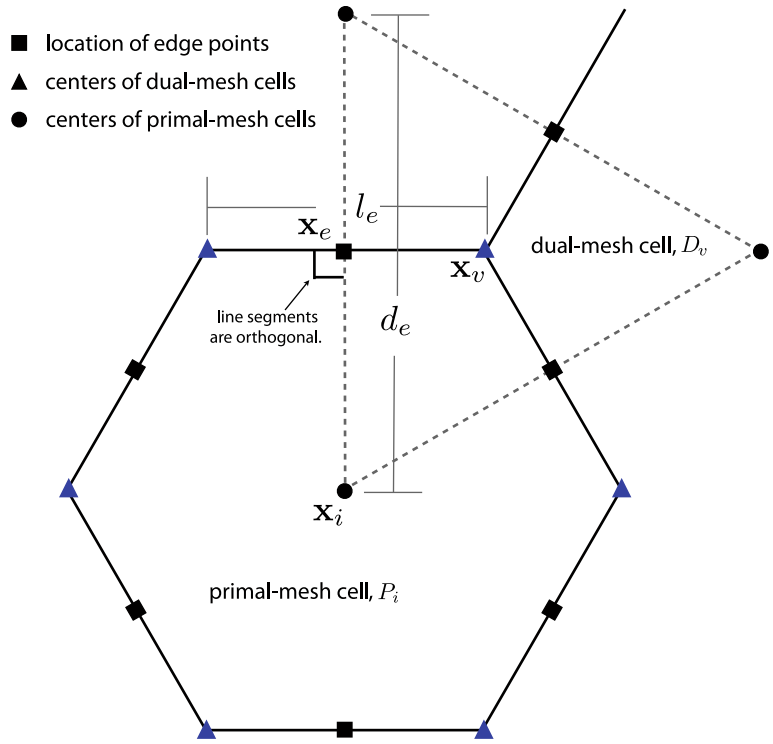

Fig. 1. Definition of elements in discrete system. Also see Table 1.

Table 1
Definition of elements used to build the discrete system.

Element	Type	Definition
$\mathbf{x}_i$	Point	Location of center of primal mesh cells
$\mathbf{x}_v$	Point	Location of center of dual-mesh cells
$\mathbf{x}_e$	Point	Location of edge points where velocity is defined
d_e	Line segment	Distance between neighboring $\mathbf{x}_i$ locations
l_e	Line segment	Distance between neighboring $\mathbf{x}_v$ locations
P_i	Cell	A cell on the primal mesh
D_v	Cell	A cell on the dual-mesh

Table 2
Definition of element groups used to build the discrete system. Examples are provided in Fig. 2.

Syntax	Output
$e \in EC(i)$	Set of edges that define the boundary of P_i
$e \in EV(v)$	Set of edges that define the boundary of D_v
$i \in CE(e)$	Two primal mesh cells that share edge e
$i \in CV(v)$	Set of primal mesh cells that form the vertices of dual mesh cell D_v
$v \in VE(e)$	The two dual-mesh cells that share edge e
$v \in VI(i)$	The set of dual-mesh cells that form the vertices of primal mesh cell P_i
$e \in ECP(e)$	Edges of cell pair meeting at edge e
$e \in EVC(v,i)$	Edge pair associated with vertex v and mesh cell i

The target primal mesh is a Voronoi diagram of the surface of the sphere. The primal mesh cell centers $\mathbf{x}_i$ are generated by recursive bisection of the icosahedron [13]. The $\mathbf{x}_i$ locations are then iteratively modified to produce a Spherical Centroidal Voronoi Tessellation (SCVT) (see [9,10]). SCVTs are a special subset of Voronoi diagrams where the $\mathbf{x}_i$ location is not only a Voronoi generator, but also the centroid of cell P_i.

It is important to note that the bisection method can lead to meshes that may or may not be Voronoi diagrams. For example, the bisection method used by [13] leads to a Voronoi diagram, while the bisection method used by [36] does not. The difference arises due to the positioning of the dual mesh centers $\mathbf{x}_v$. Confusion can arise since both [13,36] refer to their

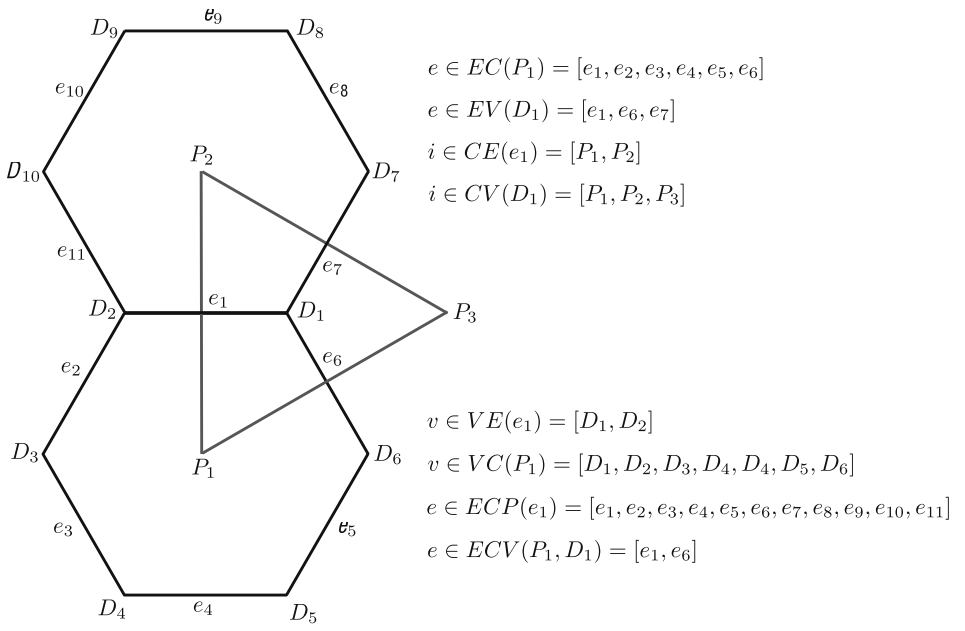

Fig. 2. Grouping of elements in discrete system. Also see Table 2.

meshes as icosahedral grids. The term "icosahedral grid" is commonly interchanged with the term "geodesic grid." While the term icosahedral grid conveys some connection to grid generation rooted to the icosahedron, the term geodesic grid is far less clear. In an attempt to avoid confusion, we simply refer to the meshes utilized herein as Voronoi diagrams; given the $\mathbf{x}_i$ locations, the mesh is uniquely specified by the Voronoi-diagram attribute. And finally, while we only exhibit the method for Voronoi diagrams that result in the quasi-uniform tessellation of the sphere, the analysis formally holds for any Voronoi/Delaunay combination as well as the other meshes mentioned in Section 1.

3.2. Equations

The discrete system is constructed starting from (2) to (7). The discrete thickness and velocity equations are expressed as

$$\frac{\partial h_i}{\partial t} = -[\nabla \cdot F_e]_i, \tag{19}$$

$$\frac{\partial u_e}{\partial t} - F_e^{\perp} \widehat{q}_e = -[\nabla(g(h_i + b_i) + K_i)]_e, \tag{20}$$

where $F_e = \widehat{h}_e u_e$ and $F_e^{\perp}$ is the thickness flux in the direction perpendicular to F_e. Eq. (20) is obtain by taking $\mathbf{n}_e \cdot$ (7) at edge locations. The manner by which we obtain $F_e^{\perp}$ is specified below. The thickness h_i, topography b_i and kinetic energy K_i are defined on the primal mesh at positions $\mathbf{x}_i$, while the velocity u_e is defined at the edge points $\mathbf{x}_e$. See Fig. 3 for more information regarding the positioning of the discrete variables. The thickness field h_i represents the mean thickness over the area spanned by primal cell i and the velocity u_e represents the component of the velocity vector in the direction normal to the primal cell edge. The $\widehat{(\cdot)_e}$ symbol represents a (yet unspecified) averaging of a field from its native location to the velocity point $\mathbf{x}_e$. Throughout the analysis we define $F_e = \widehat{h}_e u_e$ and $F_e^{\perp} = [hu]_e^{\perp}$ to represent the thickness flux per unit length in the $\mathbf{n}_e$ and $\mathbf{t}_e$ directions, respectively.

The items in (19) and (20) that require specification in order to close the system include four scalar definitions ($\widehat{h}_e, \widehat{q}_e, K_i$ and $F_e^{\perp}$) and three operator definitions ($[\nabla \times (\cdot)]_v, [\nabla(\cdot)]_e$ and $[\nabla \cdot (\cdot)]_i$).

3.3. Specification of the discrete divergence, gradient and curl operators

It turns out that the obvious choices for the discrete divergence, gradient and curl operators are also appropriate choices. Given an arbitrary thickness flux field F_e defined at the velocity points and representing the flux per unit length across the l_e edge, the divergence operator is defined at the centers of the primal mesh as

$$(\nabla \cdot \mathbf{F})_i = \frac{1}{A_i} \sum_{e \in EC(i)} n_{e,i} F_e l_e, \tag{21}$$

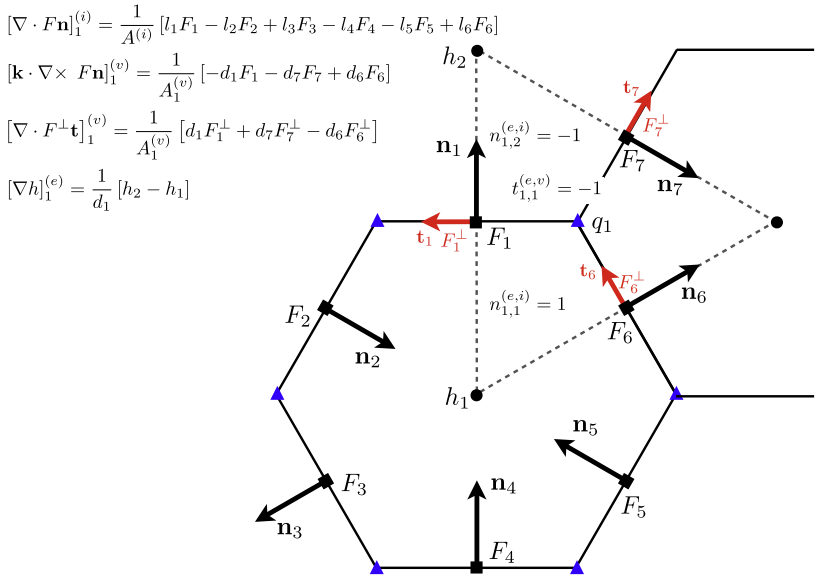

Fig. 3. Positioning of discrete variables and an illustration of discrete divergence, curl and gradient operators. Locations of discrete variables: h_i is the mean thickness associated with primal mesh cell (circles), q_v is the mean PV associated with dual mesh cell v (triangles) and u_e is the component of velocity normal to edge e (squares). In addition, kinetic energy (K_i) and topography (b_i) are also defined on the primal mesh. The variable $F_e^{\perp}$ represents the thickness flux $\widetilde{h}_e u_e$ mapped from the normal direction to the tangential direction. Note that the direction of the normal vectors $\mathbf{n}_e$ at each edge is arbitrary.

where A_i is the area of the primal mesh cell i. In order to remove the ambiguity in the sign of F_e we assume that F_e is positive when it fluxes thickness in the $\mathbf{n}_e$ direction. We also define an indicator function $n_{e,i}$, where $n_{e,i} = 1$ when $\mathbf{n}_e$ is an *outward* normal of cell i and $n_{e,i} = -1$ when $\mathbf{n}_e$ is an *inward* normal of cell i. See Fig. 3.

As shown in Fig. 3, the gradient operator is defined as

$$(\nabla h)_e = \frac{1}{d_e}\sum_{i\in CE(e)} -n_{e,i}h_i. \tag{22}$$

Similarly, the curl operator is defined as

$$\mathbf{k}\cdot(\nabla\times\mathbf{F})_v = \frac{1}{A_v}\sum_{e\in EV(v)} t_{e,v}F_e\,d_e, \tag{23}$$

where A_v is the area of the dual mesh cell v. Similar to $n_{e,i}$, the indicator function $t_{e,v}$ keeps track of whether a positive F_e makes a positive or negative contribution to the curl function at dual mesh cell v. If the vector $\mathbf{k}\times\mathbf{n}_e$ is directed toward $\mathbf{x}_v$, then $t_{e,v} = 1$. See Fig. 3 for details.

3.4. Flux mapping from the primal to the dual mesh

The breakthrough that makes this analysis possible is the robust flux interpolation scheme derived in T09. The flux interpolation scheme in T09 guarantees the following: Given an arbitrary flux field F_e defined at the velocity points and representing the flux per unit length across an l_e edge, we know via (21) that this will result in a divergence, say δ_i^F, defined at primal mesh cells. In the symbol δ_i^F the δ denotes divergence, the superscript F indicates divergence of flux "F" and the subscript i specifies the mesh on which δ^F resides. The flux interpolation scheme from T09 maps the F_e field to a $F_e^{\perp}$ field such that the divergence of $F^{\perp}$ on the dual mesh, say $\delta_v^{F^{\perp}}$, is a *convex combination* of the surrounding δ_i^F values. The specific form of the flux interpolation operator is

$$F_e^{\perp} = \frac{1}{d_e}\sum_{e'\in ECP(e)} w_{e,e'}l_{e'}F_{e'} = M(F_e). \tag{24}$$

The weights $w_{e,e'}$ in (24) are chosen such that

$$\delta_v^{F^{\perp}} = \frac{1}{A_v}\sum_{i\in CV(v)} R_{i,v}A_i\delta_i^F = I[\delta_i^F], \tag{25}$$

where $R_{i,v}$ is the weight associated with each primal-dual mesh intersection area. As shown in Fig. 4 of T09, $R_{i,v}$ represents the area of intersection between primal mesh cell P_i and dual mesh cell D_v normalized by the area of P_i. The function I denotes the manner in which the scalar divergence field on the primal mesh is mapped to the dual mesh. The consistency requirements on $R_{i,v}$ are

$$\sum_{v \in VC(i)} R_{i,v} = 1, \tag{26}$$

$$0 \leqslant R_{i,v} \leqslant 1. \tag{27}$$

The requirements that $R_{i,v}$ be bounded between zero and one and sum to one is sufficient to guarantee that the function I is a monotone interpolating function. An interpretation of (24)–(27) is that we have produced a *mapping* of an arbitrary flux field F_e directed in the $\mathbf{n}_e$ direction to a new flux field $F_e^{\perp}$ directed in the $\mathbf{t}_e$ direction such that $\delta_v^{F^{\perp}}$ is an interpolation of the δ_i^F. This relationship between $F_e^{\perp}$ and F_e is used below to develop consistent thickness and potential vorticity equations, each valid on the dual mesh.

3.5. Specification of the auxiliary discrete thickness equation

In this section we demonstrate that the properties of the flux mapping operator M defined in (24) enable the specification of an auxiliary, dual-mesh, discrete thickness equation. We begin by defining an equation for the evolution of thickness on the dual mesh having the same form as the thickness equation on the primal mesh (19) as

$$\frac{\partial h_v}{\partial t} = -\frac{1}{A_v} \sum_{e \in EV(v)} -t_{e,v} F_e^{\perp} d_e = -\left[\nabla \cdot \left(F_e^{\perp}\right)\right]_v = -\left[\nabla \cdot (M(F_e))\right]_v. \tag{28}$$

Consider the following scenario: Given an initial condition for the h_i field, generate the h_v field at $t = 0$ such that it is a monotone interpolation of the h_i field. Referring to Fig. 2 this implies that the value of $h_1^{(v)}$ is bounded by the $h_1^{(i)}, h_2^{(i)}$, and $h_3^{(i)}$ values at $t = 0$.[3] Since the function M is derived to *guarantee* that $[\nabla \cdot (M(F_e))]_v$ is an interpolation of $[\nabla \cdot F_e]_i$ for any F_e, we are assured that the RHS of (28) is always an interpolation of the RHS of (19). With the initial condition and tendency of (28) shown to be an interpolation of (19), we know that h_v is an interpolation of h_i for all time.

Alternatively, the thickness field on the dual-mesh can be determined *diagnostically*. At some time t the primal mesh thickness field is expressed as

$$h_i(t) = h_i(0) - \int_0^t [\nabla \cdot F_e]_i dt = h_i(0) - \int_0^t \delta_i^F dt. \tag{29}$$

Similarly, the dual mesh thickness field can be expressed as

$$h_v(t) = h_v(0) - \int_0^t [\nabla \cdot M(F_e)]_i dt = h_v(0) - \int_0^t \delta_v^{F^{\perp}} dt. \tag{30}$$

Using the interpolating function I in (25) to compute both $h_v(0)$ and $\delta^{F^{\perp}}$ leads to

$$h_v(t) = I[h_i(0)] - \int_0^t I\left[\delta_i^F\right] dt. \tag{31}$$

Since the interpolation operator I is additive, it commutes with the time integral to produce

$$h_v(t) = I[h_i(0)] - I\left[\int_0^t \left(\delta_i^F\right) dt\right] = I\left[h_i(0) - \int_0^t \left(\delta_i^F\right) dt\right] = I[h_i(t)]. \tag{32}$$

So the dual-mesh thickness field can be determined prognostically through the use of (30) or determined diagnostically through the use of (32); both methods will lead to the same h_v value to within round-off error. Because the dual mesh thickness field is an interpolation of the primal mesh thickness field, the order of accuracy of h_v will be determined by either the order of accuracy of h_i or the order of accuracy of the interpolation function, whichever is lower.

3.6. Specification of the discrete PV equation

In this section, we demonstrate that a discrete PV equation can be derived from the discrete velocity equation such that the velocity field and the PV field are *compatible* for all time. In addition, we demonstrate that the discrete PV equation is *consistent* with the Lagrangian property of PV by exhibiting that the discrete PV equation and an underlying thickness evolution equation have the same material derivative. The combination of compatibility and consistency leads to a discrete sys-

[3] When referencing fields with specific indices, the notation $h_1^{(i)}$ is used to make clear that the variable h is defined on the primal mesh i and the specific location is cell 1. This notation is only used for fields that reside at multiple locations.

tem where a velocity that produces a uniform PV field at $t = 0$ will evolve in such a way as to maintain a uniform PV field for all time.

As shown in (23) and Fig. 3, the discrete curl operator maps a flux field defined by normal components at edges to the centers of the dual mesh. As a result, all curl-derived quantities such as relative vorticity and PV will reside on the dual mesh. Applying the discrete curl operator defined in (23) to (20) yields

$$\frac{\partial \eta_v}{\partial t} + \frac{1}{A_v} \sum_{e \in EV(v)} -t_{e,v} F_e^{\perp} \widehat{q}_e \, d_e = 0, \tag{33}$$

where $F_e^{\perp} = M(F_e)$ with the mapping operator, M, defined in (24). Note that we have used the discrete vector identity of $\nabla \times \nabla[g(h_i + b_i) + K_i] = 0$ proven in Appendix A. As in the continuous system, we assume that the time derivative of the Coriolis parameter is zero in order to express LHS of (33) as the time tendency of absolute vorticity. We define the discrete PV as

$$q_v = \eta_v / h_v, \tag{34}$$

and substituting (34) into (33) yields

$$\frac{\partial}{\partial t}(h_v q_v) + \frac{1}{A_v} \sum_{e \in EV(v)} -t_{e,v} F_e^{\perp} \widehat{q}_e \, d_e = 0. \tag{35}$$

In order for (35) to be a valid evolution equation for q_v it is required to be consistent with an underlying thickness evolution equation; (35) must reduce identically to (28) when $q_v \equiv 1$. If we set $q_v = 1$ in (35) and require that $\widehat{q}_e = q_v$ when q_v is spatially uniform, then we find that (35) reduces to

$$\frac{\partial h_v}{\partial t} + \frac{1}{A_v} \sum_{e \in EV(v)} -t_{e,v} F_e^{\perp} \, d_e = 0 \tag{36}$$

which is identical to the evolution equation for h_v shown in (28).

This method results in an exact compatibility between the discrete momentum Eq. (20) and the discrete potential vorticity Eq. (35) in the same way that their continuous counterparts are compatible. We can obtain PV at some time, t, in two ways. In the first method we integrate (20) to time t, take the curl of the u_e field, add in the Coriolis parameter and then divide the result by h_v at time t obtained via (32). In the second method we integrate (35) to time t and divide by h_v at time t obtained via (28). The first method is a diagnostic determination of PV while the second method is a prognostic determination of PV. This analysis proves that these two estimates of PV will be identical so long as both approaches use (24) to determine $F_e^{\perp}$ and both approaches use the same method for computing $\widehat{q}_e$. We exhibit this interchangeability between the prognostic and diagnostic forms of the dual-mesh thickness and PV equations in the Section 4. The implication is that PV can be determined in a compatible, consistent and conservative manner on the wide class of meshes accommodated here while using a C-grid staggering.

3.7. Conservation of energy

We note that the above derivation of auxiliary thickness and PV equations is accomplished with only having to specify the definition of $F^{\perp}$ using (24) and requiring that $\widehat{q}_e = q_v$ when q_v is spatially uniform. The purpose of this section is to determine the appropriate constraints on the remaining three scalar degrees of freedom $(\widehat{h}_e, \widehat{q}_e, K_i)$ such that total energy is conserved in the discrete system to within time-truncation error. Perot [23] conducted a similar energy analysis for the incompressible 2D Navier–Stokes equations. The analysis conducted below extends the effort of [23] by including compressibility (by virtue of varying thickness) and by including the exchanges between potential and kinetic energy. With only minor modifications, the below analysis is applicable to the fully-compressible 2D Navier–Stokes equations.

We recognize that if this method is implemented in a 3D model based on the primitive equations, then other choices for $\widehat{h}_e, \widehat{q}_e, K_i$ might be more appropriate. Regardless, the constraint of conservation of total energy provides an excellent first approximation to these degrees of freedom. Furthermore, there is significant value in simply demonstrating that total energy can be conserved within this very general framework. Conservation of total energy is demonstrated in the discrete system in two parts. First by demonstrating that the nonlinear Coriolis force does not create or destroy kinetic energy, then by showing that the exchange of energy between its potential and kinetic forms conserves the total. Throughout the analysis a continuous-in-time system is assumed. As a result, conservation of energy is obtained to within time-truncation error.

3.7.1. Guaranteeing that $\mathbf{u} \cdot (qh\mathbf{u}^{\perp}) = 0$ in the discrete system

In the continuous system, the nonlinear Coriolis acceleration, $qh\mathbf{u}^{\perp}$, is always orthogonal to the velocity field $\mathbf{u}$. This results in the nonlinear Coriolis force neither creating nor destroying kinetic energy since $\mathbf{u} \cdot (qh\mathbf{u}^{\perp}) = 0$ for any qh and any $\mathbf{u}$. We would like the discrete system to possess this same property.

In this section, we retain only the nonlinear Coriolis force in the equation for velocity; the gradient terms will be analyzed in the following section. We demonstrate that $\mathbf{u} \cdot (qh\mathbf{u}^{\perp}) = 0$ by analyzing the coupling between any two velocity points involved in the discrete evaluation of the nonlinear Coriolis force. The result for the coupling between any two velocity points

is then generalized to the full system. Let us choose two velocity points from Fig. 3, say u_1 and u_2. Writing the evolution equation for u_1 and u_2 we have

$$\frac{\partial u_1}{\partial t} - F_1^{\perp} \widehat{q}_1 = 0, \tag{37}$$

$$\frac{\partial u_2}{\partial t} - F_2^{\perp} \widehat{q}_2 = 0. \tag{38}$$

In order to determine the time-tendency of kinetic energy due to the nonlinear Coriolis force, multiply (37) and (38) by $\widehat{h}_1 u_1$ and $\widehat{h}_2 u_2$, respectively, to obtain

$$\widehat{h}_1 \frac{\partial}{\partial t}\left(\frac{u_1^2}{2}\right) - \widehat{h}_1 u_1 F_1^{\perp} \widehat{q}_1 = 0, \tag{39}$$

$$\widehat{h}_2 \frac{\partial}{\partial t}\left(\frac{u_2^2}{2}\right) - \widehat{h}_2 u_2 F_2^{\perp} \widehat{q}_2 = 0. \tag{40}$$

Now expand $F_1^{\perp}$ and $F_2^{\perp}$ using (24) and retain only those terms in the nonlinear Coriolis force that couple u_1 and u_2 to find

$$\widehat{h}_1 \frac{\partial}{\partial t}\left(\frac{u_1^2}{2}\right) - w_{1,2} \frac{\widehat{h}_2 u_2 l_2}{d_1} \widehat{h}_1 u_1 q_{1,2} = 0, \tag{41}$$

$$\widehat{h}_2 \frac{\partial}{\partial t}\left(\frac{u_2^2}{2}\right) - w_{2,1} \frac{\widehat{h}_1 u_1 l_1}{d_2} \widehat{h}_2 u_2 q_{2,1} = 0. \tag{42}$$

Note that in (41) and (42) we have replaced $\widehat{q}_1$ and $\widehat{q}_2$ with $q_{1,2}$ and $q_{2,1}$; this allows us to introduce a symmetry into the coupling of edge 1 and edge 2 that will be necessary to prevent the nonlinear Coriolis force from creating or destroying kinetic energy. This symmetry can be expressed in terms of $q_{e,e'}$ which denotes the value of PV at edge e' used in computation of PV flux at edge e. Now multiply (41) and (42) by $A_1^{(e)}$ and $A_2^{(e)}$ and add the resulting two equations to obtain

$$A_1^{(e)} \widehat{h}_1 \frac{\partial}{\partial t}\left(\frac{u_1^2}{2}\right) - A_1^{(e)} w_{1,2} \frac{\widehat{h}_2 u_2 l_2}{d_1} \widehat{h}_1 u_1 q_{1,2} \tag{43}$$

$$+ A_2^{(e)} \widehat{h}_2 \frac{\partial}{\partial t}\left(\frac{u_2^2}{2}\right) - A_2^{(e)} w_{2,1} \frac{\widehat{h}_1 u_1 l_1}{d_2} \widehat{h}_2 u_2 q_{2,1} = 0 \tag{44}$$

where, for example, $A_1^{(e)}$ represents the yet-to-be-defined area-weighting for each u_1 velocity point. The only way to insure that time-tendency terms in (43) sum to zero is to require

$$A_1^{(e)} w_{1,2} \frac{\widehat{h}_2 u_2 l_2}{d_1} \widehat{h}_1 u_1 q_{1,2} + A_2^{(e)} w_{2,1} \frac{\widehat{h}_1 u_1 l_1}{d_2} \widehat{h}_2 u_2 q_{2,1} = 0. \tag{45}$$

From (39) in T09 we know that $w_{1,2} = -w_{2,1}$, so for arbitrary velocity and thickness fields, (45) reduces to

$$\frac{A_1^{(e)} l_2}{d_1} q_{1,2} - \frac{A_2^{(e)} l_1}{d_2} q_{2,1} = 0. \tag{46}$$

We can satisfy (46) by requiring

$$q_{1,2} = q_{2,1} \tag{47}$$

and by defining the area associated with each velocity point as

$$A_e^{(e)} = \gamma\, l_e\, d_e, \tag{48}$$

where γ is only constrained in this derivation to be any non-zero, globally-uniform constant.[4] The requirement that $q_{1,2} = q_{2,1}$ is essentially what Eq. (3) of Sadourny [26] describes as the requirement of an "energy-conserving model". By showing that the cancellation in the nonlinear Coriolis force occurs for any two edges 1 and 2, we are guaranteed that the conditions stated in (46) and (47) will lead to $\mathbf{u} \cdot (qh\mathbf{u}^{\perp}) = 0$ in the global sum.

The primary impact of (47) is to force a symmetry into the discrete system. This symmetry can be trivially satisfied by generalizing the flux mapping function in (24) to

$$Q_e^{\perp} \equiv F_e^{\perp} \widehat{q}_e = \frac{1}{d_e}\left[\sum_{e' \in ECP(e)} w_{e,e'} l_{e'} F_{e'}\left(\frac{\tilde{q}_e + \tilde{q}_{e'}}{2}\right)\right], \tag{49}$$

where $Q_e^{\perp}$ is the potential vorticity flux mapped to edge e. Eq. (49) guarantees that the nonlinear Coriolis force is energetically-neutral for *any* $\tilde{q}_e$ and *any* $\tilde{q}_{e'}$; the symmetry required by (47) is guaranteed by the $(\tilde{q}_e + \tilde{q}_{e'})/2$ functional form. In order to provide a specific example for how $\tilde{q}_e$ might be chosen, let us set

[4] The derivation of a discrete product rule in Appendix A.1 requires $\gamma = 1$.

$$\tilde{q}_e = \frac{1}{2} \sum_{v \in VE(e)} q_v, \tag{50}$$

where the variable $\tilde{q}_e$ represents the arithmetic mean of the PV values at the ends of l_e.

Notice that the $\hat{q}_e$ variable originally defined in (20) has been specified by the definitions of $F^\perp$ and $Q^\perp$. While this variable does not have to be explicitly calculated in order to close the system, for completeness we can write it as

$$\hat{q}_e = \frac{Q_e^\perp}{F_e^\perp}. \tag{51}$$

Note that each edge is associated with a unique $\hat{q}_e$. When q_v is a uniform field, (51) reduces to $\hat{q}_e = q_v$ thus resulting in a uniform PV field remaining uniform for all time in the absence of external sources or sinks.

3.7.2. Guaranteeing that the conversion of PE to/from KE is conserved

Guaranteeing a conservative exchange between kinetic and potential energy can be accomplished with two prerequisites. The first is a discrete analog to the product rule, $\nabla \cdot (\phi \mathbf{u}) = \mathbf{u} \cdot \nabla \phi + \phi \nabla \cdot \mathbf{u}$. For a general Voronoi diagram, the discrete analog to this identity was shown by Nicolaides [21] and later used by Perot [23] to shown conservation of total energy in the incompressible 2-D Navier–Stokes system. This identity is included in Appendix A.1. The second prerequisite is an averaging identity that "moves" scalar data from cell centers on the primal mesh to cell edges. This identity was a necessary part of the analysis conducted by Arakawa and Lamb [2] but was not shown. This averaging identity is derived in Appendix A.2. The process of deriving a globally-conserved energy norm allows for the specification of the final scalar degree of freedom, K_i. We omit the nonlinear Coroilis force since it is addressed immediately above.

Note that $\hat{h}_e$ is specified during the derivation of the averaging identity (A.9) and is stated as

$$\hat{h}_e = \sum_{i \in CE(e)} h_i/2. \tag{52}$$

We begin by expressing the thickness and momentum equations as

$$\frac{\partial h_i}{\partial t} + \frac{1}{A_i} \sum_{e \in EC(i)} n_{e,i} F_e l_e = 0, \tag{53}$$

$$\frac{\partial u_e}{\partial t} + \frac{1}{d_e} \sum_{i \in CE(e)} -n_{e,i} (K_i + \Phi_i) = 0, \tag{54}$$

where $F_e = \hat{h}_e u_e$ and $\Phi_i = g(h_i + b_i)$. Multiplying (54) by $A_e F_e$ gives

$$A_e \hat{h}_e u_e \frac{\partial u_e}{\partial t} + \frac{A_e F_e}{d_e} \sum_{i \in CE(e)} -n_{e,i} (K_i + \Phi_i) = 0 \tag{55}$$

and assuming a continuous-in-time system we can rewrite the time derivative as

$$A_e \frac{\partial}{\partial t} \left[\frac{\hat{h}_e u_e^2}{2} \right] - \frac{A_e u_e^2}{2} \frac{\partial \hat{h}_e}{\partial t} + \frac{A_e F_e}{d_e} \sum_{i \in G(e)} -n_{e,i} (K_i + \Phi_i) = 0. \tag{56}$$

Using (52), we can rewrite (56) as

$$A_e \frac{\partial}{\partial t} \left[\frac{\hat{h}_e u_e^2}{2} \right] - \frac{A_e u_e^2}{2} \frac{\partial}{\partial t} \left[\sum_{i \in CE(e)} h_i/2 \right] + \frac{A_e F_e}{d_e} \sum_{i \in CE(e)} -n_{e,i} (K_i + \Phi_i) = 0. \tag{57}$$

In order to focus on the kinetic energy terms, let us label

$$G_e = \frac{A_e F_e}{d_e} \sum_{i \in CE(e)} -n_{e,i} (\Phi_i). \tag{58}$$

Now sum (57) over all edges and move the term related to the geopotential to the RHS to obtain

$$\sum_e A_e \frac{\partial}{\partial t} \left[\frac{\hat{h}_e u_e^2}{2} \right] - \sum_e \frac{A_e u_e^2}{2} \frac{\partial}{\partial t} \left[\sum_{i \in CE(e)} h_i/2 \right] + \sum_e \frac{A_e F_e}{d_e} \sum_{i \in CE(e)} -n_{e,i} K_i = -\sum_e G_e. \tag{59}$$

Now use the product rule identity (A.4) to switch the sum on the kinetic energy term from over e to over i to yield,

$$\sum_e A_e \frac{\partial}{\partial t} \left[\frac{\hat{h}_e u_e^2}{2} \right] - \sum_e \frac{A_e u_e^2}{2} \frac{\partial}{\partial t} \left[\sum_{i \in CE(e)} h_i/2 \right] - \sum_i K_i \sum_{e \in EC(i)} n_{e,i} F_e l_e = -\sum_e G_e. \tag{60}$$

Now using (53) we find

$$\sum_e A_e \frac{\partial}{\partial t}\left[\frac{\widehat{h}_e u_e^2}{2}\right] - \sum_e \frac{A_e u_e^2}{4} \sum_{i \in CE(e)} \frac{\partial h_i}{\partial t} + \sum_i K_i A_i \frac{\partial h_i}{\partial t} = -\sum_e G_e. \tag{61}$$

And rearranging the second term gives

$$\sum_e A_e \frac{\partial}{\partial t}\left[\frac{\widehat{h}_e u_e^2}{2}\right] - \sum_e \sum_{i \in CE(e)} \frac{A_e u_e^2}{4} \frac{\partial h_i}{\partial t} + \sum_i K_i A_i \frac{\partial h_i}{\partial t} = -\sum_e G_e. \tag{62}$$

We can guarantee that the second and third terms in (62) cancel by defining the discrete kinetic energy as

$$K_i = \frac{1}{A_i} \sum_{e \in EC(i)} \frac{A_e}{4} u_e^2, \tag{63}$$

where we have used the fact that the summations commute. Perot [23] obtained this same discrete form for kinetic energy while developing a C-grid method for the 2-D Navier–Stokes system. For the Voronoi diagrams considered here we note that

$$A_i = \sum_{e \in EC(i)} \frac{A_e}{4}. \tag{64}$$

As a result, (63) represents a convex combination of the kinetic energies defined along the cell edges. Since the kinetic energy is evaluated based on only one of the two velocity components, the analysis indicates that the weight is doubled from 1/2 to 1. This is exactly what is found in other energy-conserving C-grid schemes on square meshes, e.g. [2,26,23].

The result of this cancellation allows us to express our kinetic energy equation as

$$\sum_e A_e \frac{\partial}{\partial t}\left[\frac{\widehat{h}_e u_e^2}{2}\right] = -\sum_e \frac{A_e F_e}{d_e} \sum_{i \in CE(e)} -n_{e,i}(\Phi_i), \tag{65}$$

where we have used (58) to expand the RHS.

Returning to the mass Eq. (53), we multiply by $A_i \Phi_i$ and sum over all cells i to obtain

$$\sum_i \Phi_i A_i \frac{\partial h_i}{\partial t} + \sum_i \Phi_i \sum_{e \in EC(i)} n_{e,i} F_e l_e = 0. \tag{66}$$

If we again assume a continuous-in-time system and expand $\Phi_i = g(h_i + b_i)$, then we can rearrange (66) to yield

$$\sum_i A_i \frac{\partial}{\partial t}[g h_i (h_i/2 + b_i)] = -\sum_i \Phi_i \sum_{e \in EC(i)} n_{e,i} F_e l_e. \tag{67}$$

Via the product rule identity (A.4) we note that

$$-\sum_i \Phi_i \sum_{e \in EC(i)} n_{e,i} F_e l_e = \sum_e \frac{A_e F_e}{d_e} \sum_{i \in CE(e)} -n_{e,i}(\Phi_i). \tag{68}$$

Thus when we add (65)–(67) the RHS will sum to zero. Doing this addition yields our discrete total energy equation as

$$\frac{\partial}{\partial t}\left\{\sum_e A_e \left[\frac{\widehat{h}_e u_e^2}{2}\right] + \sum_i A_i \left[g h_i \left(\frac{1}{2} h_i + b_i\right)\right]\right\} = 0. \tag{69}$$

The total energy of the system,

$$E = \sum_e A_e \left[\frac{\widehat{h}_e u_e^2}{2}\right] + \sum_i A_i \left[g h_i \left(\frac{1}{2} h_i + b_i\right)\right] \tag{70}$$

is conserved exactly with respect to spatial discretization. The only assumptions for this entire section are (1) continuous-in-time and (2) that an energy-conserving form of the discrete nonlinear Coriolis force is used.

The notable aspect of this analysis is that the discrete system conserves total energy in the same way that the continuous system conserves total energy: the nonlinear Coriolis force is energetically neutral, the source/sinks terms in the kinetic and potential energy equations are equal and opposite and kinetic energy is conserved under the process of transport. The result is that the discrete total energy shown in (70) is analogous to its continuous counterpart shown in (18).

3.8. Alternative choices for the potential vorticity flux

When considering the discrete formulation of the nonlinear Coriolis force, alternatives to (49) certainly exist. The long recognized, but still notable, aspect of energetically-neutral formulations of the nonlinear Coriolis force on C-grids, e.g.

(49), is that the thickness flux $F_e^\perp$ and the edge potential vorticity $\widehat{q}_e$ are intertwined; when using (49) the value of $\widehat{q}_e$ can only be determined *posto facto* through the ratio of $Q_e^\perp$ and $F_e^\perp$ shown in (51).

Regardless of how the value of $\widehat{q}_e$ is computed, the value of $\widehat{q}_e$ controls the evolution of PV, especially with regard to the evolution of higher moments of PV such as potential enstrophy. The energetically-consistent form of $Q_e^\perp$ given in (49) might not be the optimal choice from a potential enstrophy perspective.

Previous authors have argued the value of designing numerical schemes that provide some control over the potential enstrophy budget. These include schemes that conserve potential enstrophy (e.g. [26,2,6]), which must be supplemented by scale-selective dissipation terms to remove potential enstrophy from resolved scales, and schemes that inherently dissipate potential enstrophy (e.g. [27,3]). All such schemes can be accommodated within the present framework. For example a potential enstrophy conserving form of $Q_e^\perp$ is trivially obtained by first computing $\widehat{q}_e$ as

$$\widehat{q}_e = \sum_{v \in VE(e)} \frac{q_v}{2}, \tag{71}$$

then specifying $Q_e^\perp$ as

$$Q_e^\perp = F_e^\perp \widehat{q}_e. \tag{72}$$

It is a well known result that using the arithmetic mean to specify $\widehat{q}_e$ leads to conservation of the variance of q_v, e.g. [26,25,6].

Alternatively, a potential enstrophy dissipating scheme can be obtained as

$$\widehat{q}_e = \sum_{v \in VE(e)} \left| \frac{sign(F_e^\perp) - t_{e,v}}{2} \right| q_v, \tag{73}$$

and again using (72) to compute the PV flux. Eq. (73) acts as a donor-cell scheme that moves the upstream value of q_v to $\widehat{q}_e$ based on the direction of $F_e^\perp$. Both the potential enstrophy conserving and potential enstrophy dissipating schemes will, in general, act as spurious sources of kinetic energy.

3.9. Summary of the discrete analysis

In the following section we demonstrate that our choices for the four scalar definitions ($\widehat{h}_e, \widehat{q}_e, K_i$ and $F^\perp$) and three operator definitions ($[\mathbf{k} \cdot \nabla \times (\cdot)]_v, [\nabla(\cdot)]_e$ and $[\nabla \cdot (\cdot)]_i$) result in a discrete PV equation that is conservative, is consistent with an underlying thickness evolution equation and is compatible with the discrete momentum equation. In addition, total energy is conserved to within time-truncation error.

The spatial discretization of the numerical model is composed of the following prognostic equations: thickness (19) and velocity (20). These two prognostic equations specify the derived quantities of $\hat{h}_e, K_i$ and $F_e^\perp$ as (52), (63) and (24), respectively. The numerical approximations to $\nabla\cdot, \mathbf{k} \cdot \nabla\times$ and ∇ are specified in Eqs. (21)–(23), respectively. Potential vorticity on the dual mesh is computed via (34) with the dual mesh thickness calculated using (32).

Two different formulations of the nonlinear Coriolis force will be tested in the simulations discussed below. The first form is the energy-conserving form given by (49) and (50) and will be referred to as the "energy-conserving scheme". The second form is the potential enstrophy conserving form given in (71) and will be referred to as the "potential enstrophy conserving scheme".

In addition, all simulations discussed below integrate auxiliary equations. These auxiliary equations are used to demonstrate consistency between discrete prognostic and discrete derived equations. Auxiliary equations in no way impact the results of the simulation, i.e. the exact same results are obtained whether or not these auxiliary equations are simulated. Auxiliary equations for thickness evolution on the dual mesh (28) and potential vorticity evolution on the dual mesh (35) will be discussed below.

4. Results

4.1. Definition of error norms

In order to facilitate comparison to previously published error norms of shallow-water test case simulations, we specify the L_2 and L_∞ norms as

$$L_2 = \frac{\left\{ S\left[(f_n(j) - f_r(j))^2 \right] \right\}^{\frac{1}{2}}}{\left\{ S\left[(f_r(j))^2 \right] \right\}^{\frac{1}{2}}}, \tag{74}$$

$$L_\infty = \frac{\max_j |f_n(j) - f_r(j)|}{\max_j |f_r(j)|}, \tag{75}$$

where

$$S[f(j)] = \frac{\sum_{j=1}^{N_j} f(j)A(j)}{\sum_{j=1}^{N_j} A(j)}. \tag{76}$$

The function $f_n(j)$ is the numerical solution defined at the $\mathbf{x}_j$ positions on the numerical mesh. The index j can represent the cells on the primal or dual mesh. The function $f_r(j)$ is the reference solution that has been calculated at or interpolated to the same $\mathbf{x}_j$ positions. The reference solution represents either an analytic solution or, if an analytic solution is not available, a high-resolution solution that is sufficiently accurate for the computation of the error norms. The function $S[f]$ computes the global average of f where A_j is the area associated with cell j. The function $\max_j|f|$ finds the global maximum of the $|f|$ evaluated at the $\mathbf{x}_j$ positions of the numerical mesh.

4.2. Description of numerical simulations

Three of the test cases from the standard shallow-water test case suite from Williamson et al. [37] are conducted to confirm the analytical findings above. The simulations are conducted with four spatial resolutions: 2562, 10,242, 40,962 and 163,842 Voronoi cells, corresponding to spatial resolutions of approximately 480 km, 240 km, 120 km and 60 km, respectively. As indicated above, the specific form of Voronoi diagram used is a Spherical Centroidal Voronoi Diagram. The time stepping for all simulations is a 4th-order Runge–Kutta scheme. The time steps for the simulations are 200 s, 144 s, 100 s, and 72 s corresponding to the 2562, 10,242, 40,962 and 163,842 spatial meshes, respectively. All results presented below, including error norms, are essentially independent of time step lengths between 50 s and 200 s for these simulations. All simulations are conducted with 64-bit floating point arithmetic.

4.3. Test Case 2: Global steady state nonlinear geostrophic flow

Test Case 2 (TC2) uses the full nonlinear shallow-water equations with a perfectly balanced initial condition resulting in steady-state nonlinear geostrophic balance. Since the initial condition is an exact solution of the shallow-water equations, any departure of the numerical simulation from the initial condition is error due to discretizing the continuous system. The initial height and velocity field have the form

$$gh = gh_0 - \left(a\Omega u_0 + \frac{u_0^2}{2}\right)\cos\theta, \tag{77}$$

$$u = u_0 \cos\theta. \tag{78}$$

Following [37], the physical parameters of the system are $\Omega = 7.292 \times 10^{-5}\ \mathrm{s}^{-1}$, $g = 9.80616\ \mathrm{m\,s}^{-2}$ and $a = 6.37122 \times 10^6$ m. Latitude is denoted by θ, $gh_0 = 2.94 \times 10^4\ \mathrm{m}^2\ \mathrm{s}^{-2}$ and $u_0 = 2\pi a/(12\,days)$.

TC2 is simulated for 365 days with 40962 Voronoi cells using both the energy and potential enstrophy conserving schemes. Fig. 4 measures the energetic consistency of each simulation by plotting the kinetic energy doubling time as

$$\text{Time to Kinetic Energy doubling} = \frac{S[h_i K_i]}{\left|S\left[\frac{dE}{dt}\right]\right|}, \tag{79}$$

where K and E are defined in (63) and (70), respectively. The time derivative is approximated by $(E(n+1) - E(n))/dt$. Eq. (79) measures the time-scale over which we expect the simulation to remain bounded with respect to energetic consistency. The energy-conserving simulation exhibits essentially inviscid, stable dynamics with a "time to doubling" of $O(10^4$ years). The potential enstrophy conserving scheme shows significant oscillations on the time scale of a day with an average time-to-doubling of $O(10^3$ years). For this test case, both the energy and potential enstrophy conserving schemes exhibit an energetic consistency that is more than sufficient for a realistic representation of the continuous system.

The analysis in Section 3 pays particular attention to the role of the nonlinear Coriolis force in the system energetics. During the one year simulation, the maximum contribution to the global mean kinetic energy budget is $1.0 \times 10^{-14}\ \mathrm{m}^3\ \mathrm{s}^{-3}$ when using the energy-conserving scheme, thus confirming that the discrete nonlinear Coriolis force shown in (49) is energetically neutral to within round-off error. The potential enstrophy conserving scheme exhibits trends in the global mean kinetic energy budget of approximately $1.0 \times 10^{-4}\ m^3\ s^{-3}$ during the one year simulation.

Fig. 5 measures the L_2 and L_∞ error norms of the thickness field as a function of time when using the energy conserving scheme. Both error norms show oscillations due to gravity waves pushing the numerical solution toward and away from the analytic solution. The L_2 and L_∞ error norms have characteristic values of 2.0×10^{-5} and 4.0×10^{-4}, respectively.

Fig. 6 measures the discrepancy between the auxiliary, prognostic evaluation of thickness and PV on the dual mesh versus the diagnostic evaluation of these same quantities. As expected from the analysis in Section 3, the prognostic and diagnostic evaluation of thickness and PV on the dual mesh differ at the level of round-off error. At $t = 0$ the error is approximately 1.0×10^{-14}. As time progresses, the error grows to approximately 1.0×10^{-10}. Note that the L_∞ error measures the largest discrepancy between the auxiliary and diagnostic evaluation for all dual-mesh cells. While not discussed further, this result also holds for all simulations presented below.

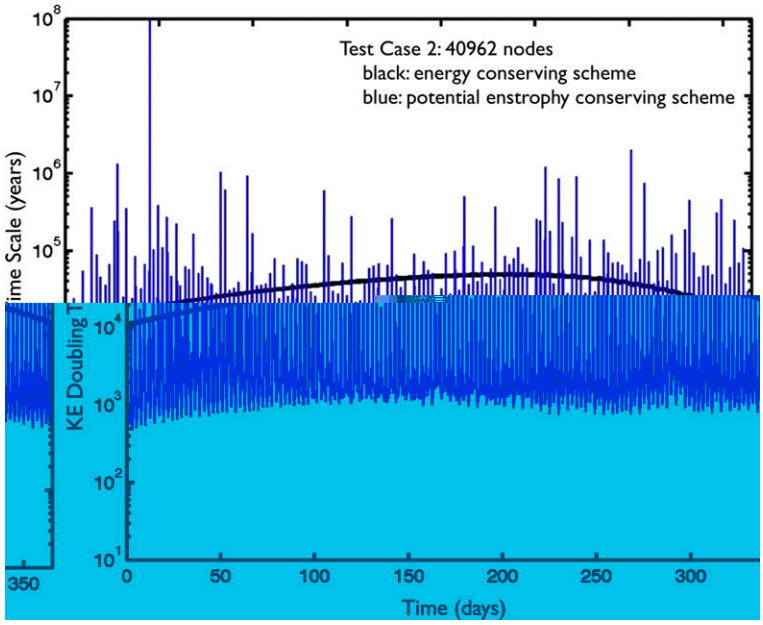

Fig. 4. The time-scale for doubling global mean kinetic energy as defined in (79).

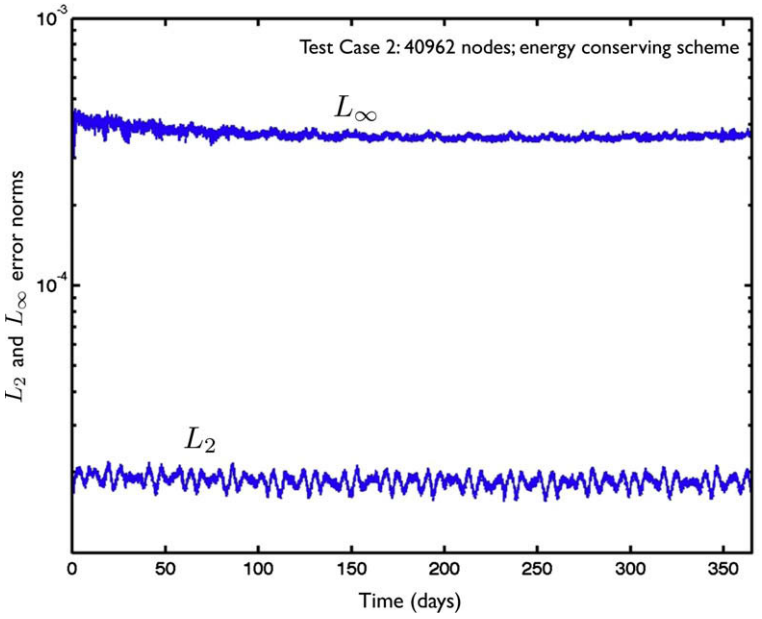

Fig. 5. Error norms at a resolution of 40,962 over the course of a one year simulation.

The standard configuration of TC2 calls for a simulation of 12 days, corresponding to one rotation of the fluid flow around the sphere. Fig. 7 shows the L_2 and L_∞ error norms based on the thickness field of the simulation at day 12 for resolutions of 2562, 10,242, 40,962 and 163,842 when using the energy-conserving scheme. The L_2 error norm exhibits a convergence rate of approximately 1.5 with respect to nominal grid spacing, indicative of a method between 1st- and 2nd-order accuracy. The L_∞ error norm shows little convergence with increasing resolution. The discrete system obtains a geostrophic balance that results in an $O(1)$ error in the vicinity of the midlatitude primal mesh pentagons. Fig. 7 also shows the L_2 and L_∞ error norms when using the potential enstrophy conserving scheme with 40,962 nodes. The norms are only slightly degraded when using the potential enstrophy conserving scheme. Overall, the norms are comparable to previously published results utilizing finite-volume methods discretized on similar meshes, such as [13,17,36].

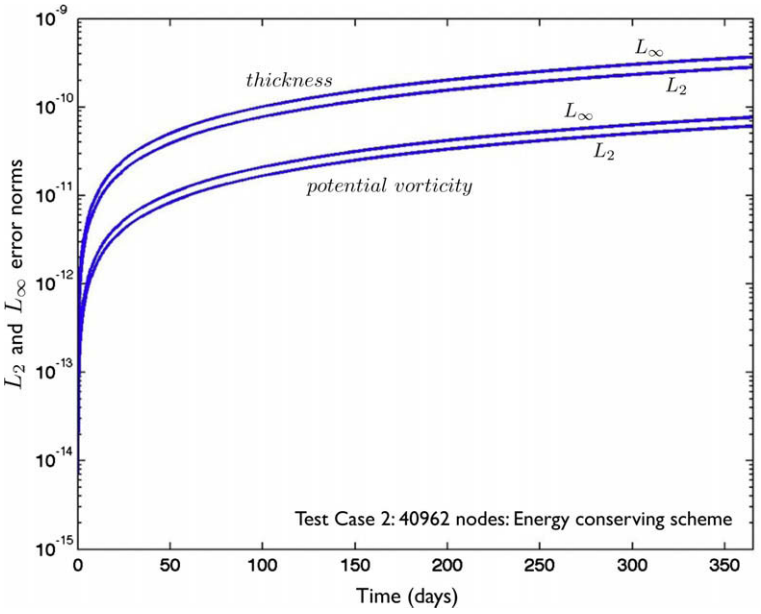

Fig. 6. Discrepancy between the prognostic and diagnostic evaluation of thickness and PV on the dual mesh at a resolution of 40,962 over the course of a one year simulation.

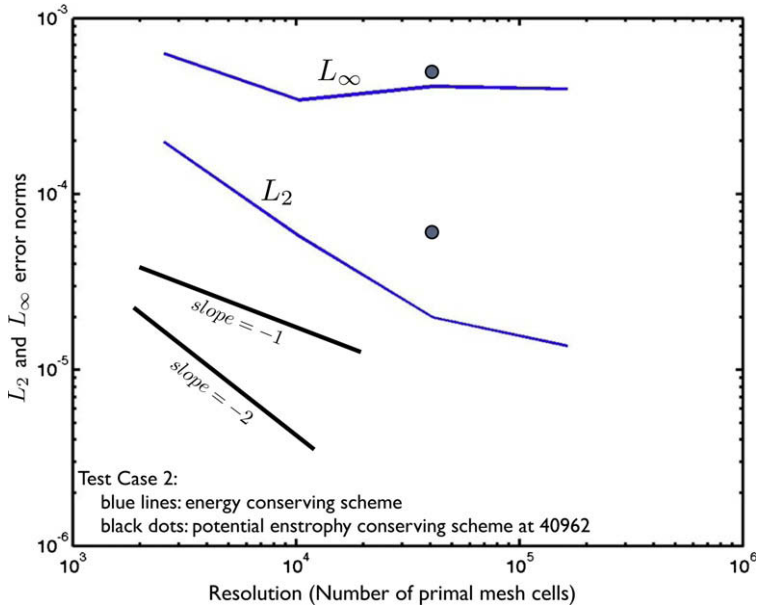

Fig. 7. Convergence rate of TC2 as measured by the L_2 and L_∞ norms based on the thickness field. Norms are computed with respect to analytic solution. The reference slopes of -1 and -2 are with respect to nominal grid resolution.

4.4. Test Case 5: Zonal flow over an isolated mountain

Test Case 5 (TC5) in [37] has a similar initial condition as TC2, except $h_0 = 5960$ m and $u_0 = 20$ m s^{-1}. In addition, an isolated mountain of the form

$$b = b_0\left(1 - \frac{r}{R_0}\right) \tag{80}$$

is included at the lower boundary with $b_0 = 2000$ m, $R_0 = \pi/9$ and $r^2 = \min[R^2, (\lambda - \lambda_c)^2 + (\theta - \theta_c)^2]$ where λ is longitude. In this test case, $\lambda_c = -\pi/2$ and $\theta_c = \pi/6$. The fluid thickness is adjusted so that the topographic height plus the fluid thickness

is equivalent to the total depth specified in (77) with $h_0 = 5960$ m and $u_0 = 20$ m s^{-1}. Large amplitude Rossby and gravity waves are forced as the geostrophically-balanced velocity field is forced to rise or circumvent the topographic feature.

Since TC5 does not have a known analytic solution, error norms are computed with respect to a T511 global spectral model [31]. For TC5 at T511, the global spectral model requires a scale-selective ∇^4 dissipation of 8.0×10^{12} m^4 s^{-1} in order to prevent the accumulation of energy and potential enstrophy at the grid scale. The L_2 and L_∞ error norms based on the thickness field at day 15 are shown in Fig. 8 when using the energy-conserving scheme. The L_2 and L_∞ error norms exhibit convergence rates of approximately 1.6 and 1.5, respectively, with respect to the nominal grid spacing. These error norms are essentially identical to [17] and compare quite favorably to [36]. As indicated in Fig. 8, the error norms are only slightly degraded when using the potential enstrophy conserving scheme.

Fig. 9 shows the errors in globally-average potential enstrophy that result when using the energy-conserving numerical scheme. Increasing resolution leads to better conservation of potential enstrophy. The simulations all show reductions in potential enstrophy from hour 0 to hour 40. After hour 40 the simulations show increases in potential enstrophy. For long-time stability in TC5, the secular increase in potential enstrophy will need to be controlled through some form of closure. The potential enstrophy conserving scheme exhibits conservation of globally-integrated potential enstrophy out to at least 20 digits and well within the realm of round-off error.

The other aspects of this TC5 simulation are similar to TC2. In particular, the kinetic energy doubling time for the energy-conserving scheme is uniform in time, but reduced in magnitude, with values $O(10^1$ years) in all four simulations. The nonlinear Coriolis force is energetically-neutral with contributions to the kinetic energy tendency of approximately 1.0×10^{-13}. The potential enstrophy conserving simulations show kinetic energy doubling times of $O(10^0$ years) with contributions to the kinetic energy tendency of approximately 1.0×10^{-1}). In all simulations the error between the auxiliary, prognostic evaluation of thickness and PV on the dual mesh versus the diagnostic evaluation of these quantities is of the size of round-off error.

While the discrete nonlinear Coriolis force is energetically neutral to within round-off error, the energy conversion terms shown on the RHS of (67) and (68) are only conserved to within time-truncation error. Due to the large transient forcing at $t = 0$ in TC5, this test case can be used to confirm that the numerical scheme does conserve total energy in the limit $dt \to 0$. TC5 is simulated for one day with 2562 Voronoi cells and time steps ranging from 1800 s to 1 s. Over this range of time step lengths, the kinetic energy doubling time scale shown in (79) increases uniformly from 3.0×10^2 days with $dt = 1800$ s to 5.0×10^5 days with $dt = 1$ s. The increase in doubling time scale is due almost entirely to better approximations of the energy conversion terms with decreasing time step. As a result, we conclude that the numerical scheme conserves total energy to within time truncation error.

4.5. Test Case 6: Rossby–Haurwitz wave

This test case is a zonal wavenumber 4 Rossby–Haurwitz wave. The initial state is an exact steadily propagating solution of the nondivergent shallow-water equations. The specification of this test case is provided in [37, Eqs. (141)–(149)]. We

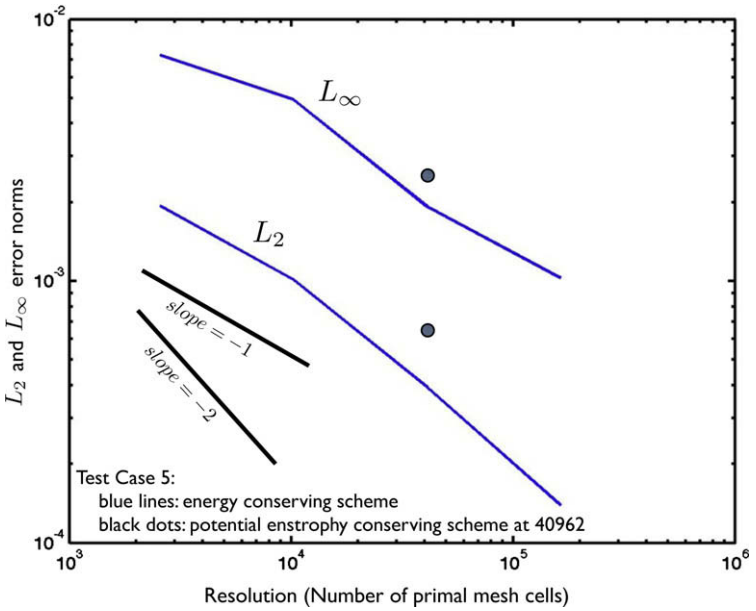

Fig. 8. Convergence rate of TC5 as measured by the L_2 and L_∞ norms based on the thickness field. Norms are computed with respect to T511 global spectral model solution. The reference slopes of −1 and −2 are with respect to nominal grid resolution.

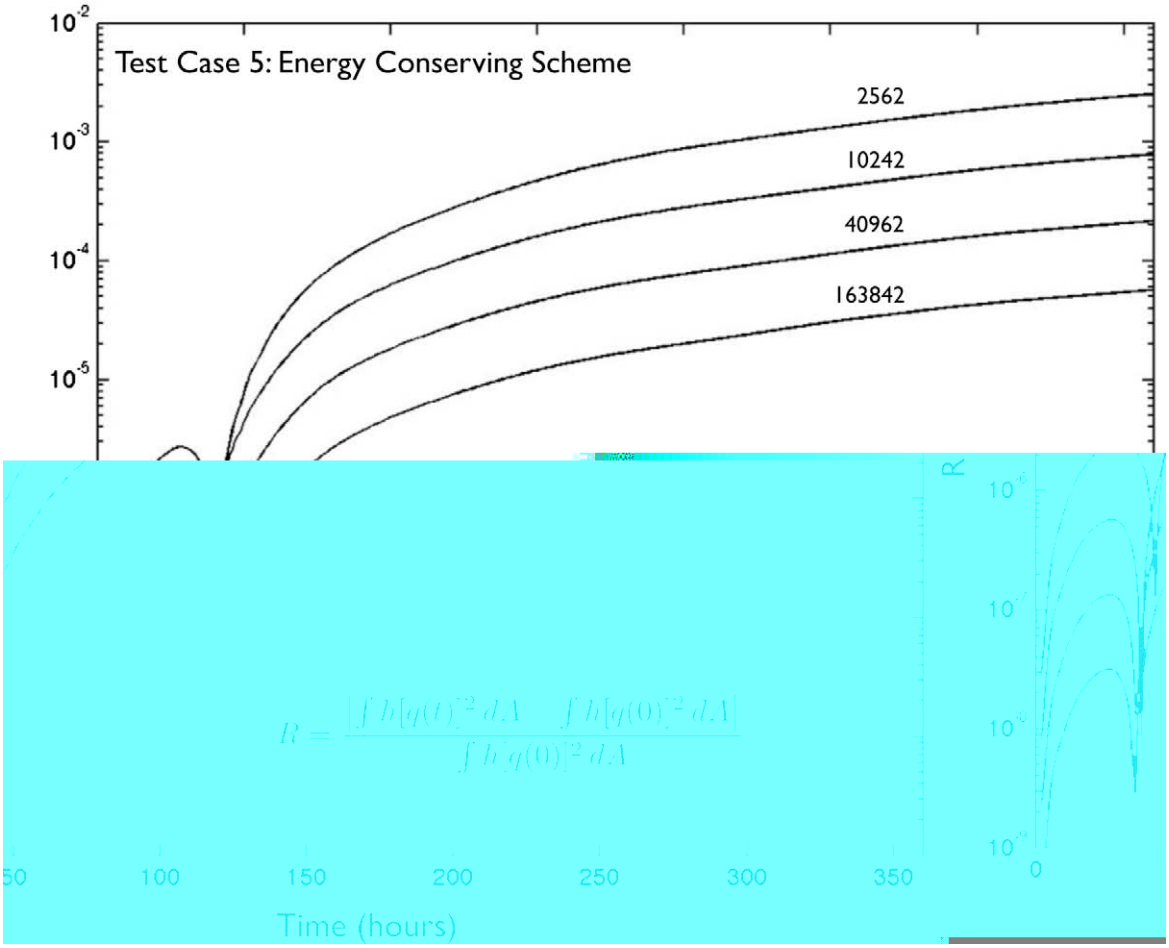

Fig. 9. Fractional error in potential enstrophy conservation for the energy-conserving scheme.

integrated the test case for 14 days as suggested in [37]. Since TC6 is not an exact solution of the full nonlinear shallow-water equations, we use a T511 global spectral model simulation as the reference solution. As with TC5, the global spectral model requires a ∇^4 dissipation in order to control noise at the highest wave numbers. For TC6 we use $5.0 \times 10^{12}\, m^4\, s^{-1}$ as the coefficient for the ∇^4 dissipation. The L_2 and L_∞ error norms based on the thickness field of the energy conserving scheme are shown in Fig. 10. Both error norms show a convergence rate of approximately 1.9 with respect to the nominal grid spacing, indicative of a 2nd-order accurate scheme. In terms of absolute accuracy, the simulations are comparable to [13] and significantly better than [36]. Fig. 10 also shows the L_2 and L_∞ error norms of the potential enstrophy conserving scheme. In this case, the errors associated with the potential enstrophy scheme are significantly higher than those found for the energy conserving scheme. The other aspects of this simulation related to conservation are essentially identical to that discussed for TC5.

5. Discussion

The primary complication with the C-grid method arises during the consideration of the discrete system's PV dynamics. By construction, the C-grid method staggers the mass and vorticity fields, with mass defined at the centers of the primal mesh and vorticity defined at the centers of the dual mesh. Since shallow-water PV is defined as the ratio of vorticity to fluid thickness, it is not immediately obvious how, or even where, to define PV when using a C-grid staggering.

By extending the results of [35] to the nonlinear shallow-water equations, we overcome this complication regarding PV dynamics when using a C-grid staggering. The technique developed in [35] allows for the reconstruction of the tangential velocity field such that the divergence on the dual mesh is an interpolation of the divergences on the neighboring primal mesh cells. By extending this idea to the consideration of mass fluxes, we are able to derive a thickness equation on the dual mesh that is guaranteed to be an interpolation of the thickness equation defined on the primal mesh. We thereby circumvent the basic problem with C-grid methods by obtaining a dual mesh thickness equation that is collocated with the vorticity

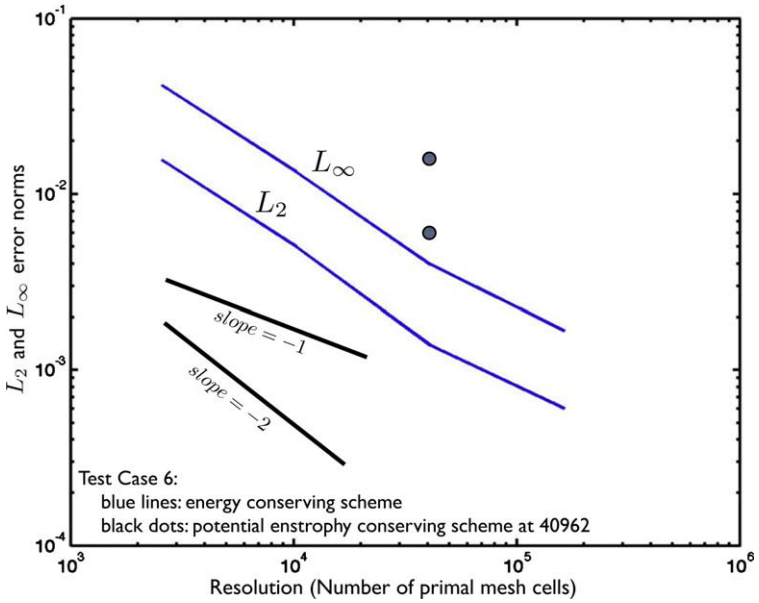

Fig. 10. Convergence rate of TC6 as measured by the L_2 and L_∞ norms based on the thickness field. Norms are computed with respect to T511 global spectral model solution. The reference slopes of -1 and -2 are with respect to nominal grid resolution.

field. We refer to the dual-mesh thickness equation as the auxiliary thickness equation. While the auxiliary equation is "extra" in the sense that it is not required to constrain the thickness field, it proves critically important for the specification of PV.

Fundamental to conserving PV with a C-grid method is the existence of an auxiliary thickness equation defined on the dual mesh. Previous efforts to derive PV conservation using a C-grid staggering have addressed this issue both indirectly and directly. An auxiliary thickness equation defined on the dual mesh is inferred by Sadourny [26] with the specification of the discrete form of PV (p. 682) and shown explicitly by Arakawa and Lamb [2] in Eqs. (3.15) and (3.16). While neither demonstrate that their auxiliary, dual-mesh thickness equation is a valid interpolation of the primal mesh thickness equation, both in fact are appropriate interpolations. In fact, the weights used in [2] to specify the auxiliary thickness equation are precisely the weights we derived as $R_{i,v}$ shown in (25). The key feature of the method developed here is the knowledge of the thickness fluxes that lead to the dual-mesh thickness equation being an interpolation of the primal mesh thickness equation; without knowledge of these fluxes, a valid PV equation cannot be constructed.

The contribution here is that the technique to specify the auxiliary thickness equation holds for a wide class of meshes beyond the square and lat-lon meshes considered in [2]. In addition to square and lat-lon meshes, meshes formally included in the derivation are Voronoi diagrams, Delaunay triangulations, and conformally-mapped cubed-sphere meshes. The ability to construct robust algorithms on a wide range of meshes using a C-grid staggering opens up new avenues of research that are detailed further below.

The ability to construct a valid dual-mesh thickness equation is only the first step in developing a robust numerical scheme with regard to PV dynamics. We must also be able to guarantee that the curl of the momentum equation leads to the appropriate form of the vorticity equation. One way to facilitate the formulation of the discrete vorticity equation is to discretize the vector-invariant form of the momentum equation shown in (5). When the vector-invariant form of the momentum equation is discretized on an arbitrarily-structured C-grid staggering, it is fairly straightforward to show that the gradient terms will be curl-free (see Section A.3), as is the case for the continuous system. Other than the gradient terms, the only other source term in the momentum equation is the nonlinear Coriolis force (7). The curl of the nonlinear Coriolis force is shown to be equivalent to the flux of PV in the tangential direction (12). Furthermore, it is shown that the sole tendency term of the PV equation defined on the dual-mesh grid is the divergence of the nonlinear Coriolis force.

The result of the analysis is the formulation of a discrete, dual-mesh PV equation that is *compatible* with the underlying momentum equation and *consistent* with the Lagrangian property of PV. The compatibility with the momentum equation results from the ability to derive the discrete PV equation from the discrete momentum equation. Consistency with the Lagrangian property of PV is when the discrete system possesses an analog to (1) in the sense that the discrete PV field evolves with the same material derivative as the underlying continuity equation from which the PV is derived. A scheme that is consistent in this manner has a discrete PV equation that reduces identically to the discrete thickness equation when the PV field is spatially uniform.

Other recent works have attempted to obtain the PV properties of compatibility and consistency through different means. Notably, Lin and Rood [16] define PV on the primal mesh instead of the dual mesh. One of the primary motiva-

tions for Lin and Rood to define absolute vorticity (and PV) on the primal mesh instead of the dual mesh is to insure that PV is accompanied by a valid thickness equation, i.e. to preserve the correlation between thickness flux and PV-weighted thickness flux. In fact, Lin and Rood conclude that "To achieve the goal of transporting h (mass) and Ω (absolute vorticity) by exactly the same manner, an obvious requirement is that h and Ω be defined at the same point (or, in the finite-volume sense, enclosed in the same cell)." While the correlation between thickness flux and PV-weighted thickness flux is clearly preserved by collocating thickness and PV on the primal mesh, the present analysis suggests that collocation on the primal mesh is not a requirement. The collocation of thickness and PV on the primal mesh comes at possibly considerable cost. The analysis from Skamarock [28] demonstrates that the positioning of PV on the primal mesh results in creation of a null space in the divergence field. Anecdotal evidence indicates that this null space must be controlled through the application of explicit divergence damping (Jablonowski, personal communication). It would appear that many of the issues that arise when thickness and PV are collocated on the primal mesh can be remedied by the use of the technique developed here.

Simulations of test cases 2, 5, and 6 from the Williamson et al. [37] shallow-water test case suite confirm the analysis in Section 3. Specifically the simulations confirm that the derived auxiliary dual-mesh thickness equation is a valid interpolation of the primal mesh thickness equation. Whether obtained through prognostic or diagnostic evaluation, thickness at a dual-mesh cell is always bounded by the thicknesses at the neighboring primal mesh cells (see Fig. 6). This relationship holds to round-off error. The long-time stability of the test cases (in particular test case 2 that was integrated for 365 days) demonstrates that no spurious sources of PV are present in the numerical scheme, thus PV is both consistent with its underlying dual-mesh thickness equation and compatible with its underlying momentum equation. As a result, all simulations conserve globally-integrated PV to within round-off error. The simulations utilizing the energy-conserving form of PV flux shown in (49) exhibit energy conservation to within time-truncation error. Overall, the conservation of discrete PV and energy is orders of magnitude beyond that required to faithfully mimic the physical system [34].

In addition to evaluating the conservation properties in test cases 2, 5, and 6, the accuracy of those simulations is also presented. In terms of order of accuracy, the scheme shows convergence rates between 1st- and 2nd-order accuracy. For example, the L_2 and L_∞ norms for test case 5 are nearly identical to Lipscomb and Ringler [17] and slightly better than Tomita et al. [36]. The results from test case 2 are also comparable to these other works with the exception of the L_∞ norm that fails to converge. We have traced this issue to the fact that the velocity field is not centered on the primal mesh cell edge. This issue might be resolved by adopting mesh generation techniques developed in [36] or [13]. The results of test case 6 compare favorably to other finite-volume simulations with error norms nearly identical to [13] and approximately a factor of four better than [36]. Overall, we judge the order of accuracy of the numerical scheme to be typical of finite-volume schemes discretized on a quasi-uniform mesh of the sphere.

Section 4 presents results using an energy conserving and a potential enstrophy conserving scheme. Overall, we judge the shallow-water test cases to not be sufficiently discriminating to make a clear choice between the two schemes. Both schemes exhibit long-time stability for TC2, showed similar error norms and were able to complete all simulations without the need for *ad hoc* dissipation to preserve stability. As discussed below, each scheme has extensions that we are currently exploring.

The first extension of the method is to alter the manner in which the PV-flux, $Q_e^\perp$, is computed in order to guarantee both energy conservation and potential enstrophy dissipation. We have a significant amount of freedom in the energy-conserving formulation of $Q_e^\perp$; the $Q_e^\perp$ defined in (49) is energy conserving for *any* $\tilde{q}_e$ where $\tilde{q}_e$ is PV defined on cell edges. The approach is then to determine the suitable $\tilde{q}_e$ values that lead to the appropriate rate of potential enstrophy dissipation. In spirit, this idea is essentially the "Anticipated Potential Vorticity Method" (APVM) of Sadourny and Basdevant [27] implemented on arbitrarily-structured C-grids. We have already begun experimenting with an APVM-approach by incorporating an upstream bias in (50) to yield

$$\tilde{q}_e = \frac{1}{2}\sum_{v\in VE(e)} q_v - \frac{1}{2}\left(\mathbf{u}_e \cdot [\nabla q]_e\right) dt, \tag{81}$$

where dt is the time step. The energy-conserving method is implemented exactly as described above, except (81) is used in place of (50). The initial testing is extremely promising. In TC2 the APVM has virtually no impact on the solution since $\mathbf{u}_e$ and $[\nabla q]_e$ are perpendicular; error norm, energy conservation and potential enstropy conservation values are essentially unchanged. In TC5 the APVM allows for long-time stability of the numerical simulation while conserving total energy. Fig. 11 shows the relative vorticity field from an APVM simulation along with the relative vorticity obtained from the baseline energy-conserving simulation at day 50 for TC5. The APVM produces coherent structures in the vorticity field at day 50, even as strong filamentation occurs. In contrast, the baseline energy-conserving method is beginning to exhibit a breakdown in the relative vorticity field by day 50; this breakdown continues and by day 100 the vorticity field is composed almost entirely of noise. The APVM simulation retains a coherent vorticity structure until the end of the 150 day integration. Over the course of this 150 day simulation the APVM scheme dissipates potential enstrophy with a characteristic time scale of approximately 100 days. The one key ingredient missing from this implementation of the APVM is a rigorous proof that the method dissipates potential enstrophy for a general flow. Based on these preliminary results, we deem it likely that the degree of freedom in the specification of $\tilde{q}_e$ can be used to dissipate potential enstrophy on time-scales consistent with the physical system [34]. With this approach we would be using the freedom in $\tilde{q}_e$ to control the rate at which potential enstrophy moves from the resolved scales to the unresolved scales.

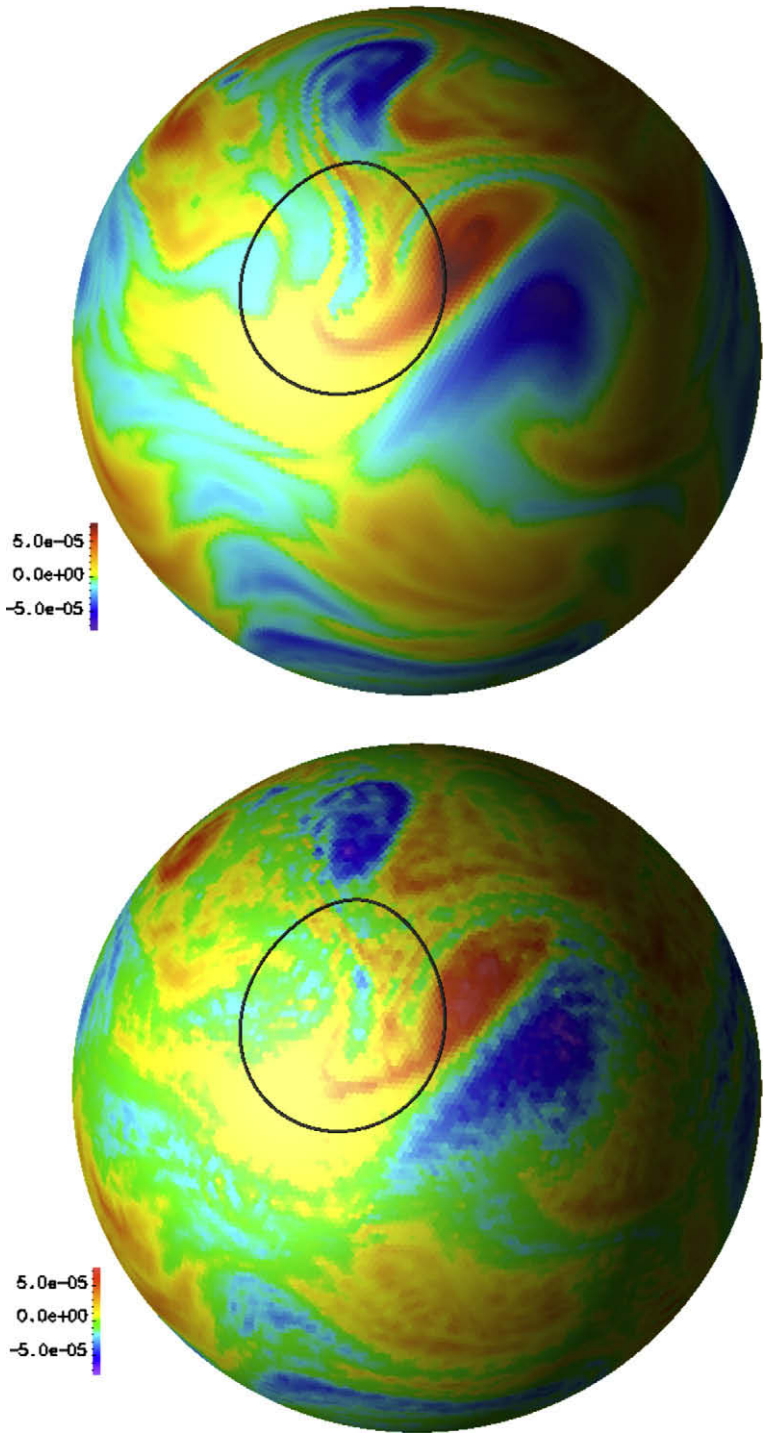

Fig. 11. TC5 at day 50 using 40962 cells. Top: Relative vorticity from the APMV method (using (81)). Bottom: Relative vorticity from the baseline energy-conserving method (using (50)). The color bars are identical and have been chosen to emphasize the filament structure of the flow.

The second extension of the PV-flux computation is directed toward the idea of high-order transport. This is very similar to the approach of Lin and Rood [16], except here the PV is defined on the dual mesh. The dual-mesh PV equation shown in (35) can be solved using essentially any finite-volume transport algorithm. So long as the PV fluxes resulting from this transport algorithm are used to evolve the momentum equation shown in (20), the evolution of momentum and PV will remain compatible to within round-off error as shown in Fig. 6. The one caveat here is that the dual-mesh thickness flux is specified

in (24). As a result, the high-order approximations of PV-flux will essentially be obtaining more accurate approximations to $\widehat{q_e}$ shown in (71). The notable aspect of this approach is that the rotational modes of the velocity field will evolve with the same order of accuracy as the PV equation. Say, for example, that the PV-flux is computed with 4th-order accuracy and that this estimate of $Q_e^{\perp}$ is used to time step the momentum equation in (20). The velocity is thus constrained to evolve with rotational modes consistent with 4th-order accuracy in PV. The remarkable result is that it is possible to utilize the wealth of knowledge related to finite-volume transport to constrain the evolution of a momentum equation that is not written in flux form. We are currently exploring various techniques for implementing high-order, flux-form transport schemes on arbitrarily-structured C-grids.

And finally in closing, the algorithm developed above is valid for variable-resolution meshes. Since the conservation properties related to energy and PV are equally valid on variable-resolution meshes, we can begin to contemplate the notion of regional increases in resolution for atmosphere and ocean modeling within the framework of global system modeling. The idea is to locally enhance resolution while maintaining a simulation for the global system. While a whole spectrum of issues arises when considering this idea, such as the requirement for scale-aware physical parameterizations, reduction in formal order of accuracy and spurious wave reflection across mesh transition zones, it appears that we have overcome the significant hurdle related to energy and PV conservation for variable-resolution meshes applied to geophysical fluid problems. As a result, the method outlined above provides one path forward toward exploring the value of variable-resolution methods for the simulation of the global atmosphere and ocean systems.

Acknowledgments

The careful review provided by three anonymous reviewers led to significant improvements to this contribution. This work was supported by the DOE Office of Science's Climate Change Prediction Program DOE 07SCPF152. NCAR is supported by the National Science Foundation. We would like to thank Lili Ju for generating the meshes used for the simulations presented in Section 4.

Appendix A. Discrete algebraic and vector identities

The analysis to be completed in this appendix includes the proof of three identities: the product rule identity, an averaging identity and the $\nabla \times \nabla h = 0$ identity. The first two identities are required for the analysis of the discrete energy equation, while the last identity is required for the derivation of the discrete PV equation.

A.1. Product rule identity

In the continuous system the following vector identity exists:

$$\nabla \cdot (h\mathbf{u}) = h\nabla \cdot \mathbf{u} + \mathbf{u}\nabla h. \tag{A.1}$$

If we integrate (A.1) over the singly-connected surface of the sphere S such that the LHS vanishes, we are left with

$$\int_S h\nabla \cdot \mathbf{u} dS = -\int_S \mathbf{u}\nabla h dS. \tag{A.2}$$

We require that the discrete analog of (A.2) holds, namely that

$$\sum_i h_i (\nabla \cdot u_e \mathbf{n}_e)_i A_i = -\sum_e u_e \mathbf{n}_e \cdot (\nabla h_i)_e A_e, \tag{A.3}$$

where the discrete divergence and gradient operators are given in (21) and (22), respectively.

Substituting the discrete operators defined in (21) and (22) into (A.3) we find

$$\sum_i h_i A_i \left[\frac{1}{A_i}\sum_{e\in EC(i)} n_{e,i} u_e l_e\right] = -\sum_e \frac{u_e A_e}{d_e}\left[\sum_{i\in CE(e)} -n_{e,i} h_i\right]. \tag{A.4}$$

While the identity only needs to be satisfied in the global sum, we will require the cancellation to occur at every cell edge. We choose, without loss of generality, to evaluate (A.4) for $e = 1$ and the associated cell centers $i = 1$ and $i = 2$ as shown in Fig. 3. We expand (A.4) and retain only terms that couple $e = 1$ to $i = 1$ and $e = 1$ to $i = 2$ to find

$$h_1^{(i)} u_1 l_1 - h_2^{(i)} u_1 l_1 = \frac{u_1 A_1^{(e)}}{d_1}\left(h_1^{(i)} - h_2^{(i)}\right). \tag{A.5}$$

Eq. (A.5) will be satisfied if and only if

$$A_e = l_e d_e. \tag{A.6}$$

When the primal mesh is a Voronoi diagram, as considered here, the unique area associated with each edge is equal to $l_e d_e/2$. This unique, diamond-shaped area is obtained by connecting the two primal mesh cell centers and the two dual-mesh cell

centers associated with edge e. The area-weighting required to satisfy the discrete product rule is twice that of the unique area associated with that edge. The factor of two arises because the C-grid staggering retains only the portion of the product rule in the $\mathbf{n}_e$ direction. The weights obtained here are identical to those used in [2] for a square mesh.

The area associated with a primal mesh cell is chosen as

$$A_i = \sum_{i \in CE(e)} \frac{A_e}{4} \tag{A.7}$$

so that A_i sum to the physical area of the domain.

A.2. Averaging identity

We require the following to be true:

$$\sum_i h_i \widehat{g_e} A_i = \sum_e \widehat{h_i} g_e \frac{A_e}{2}, \tag{A.8}$$

where h_i is a scalar field defined on the primal mesh, g_e is a scalar field defined at edges e, A_i is the area of cell i given in (A.7) and A_e is the area associated with edge e given by (A.6). The form of (A.8) is chosen to be consistent in the sense that when $h_i \equiv 1$ and $g_e \equiv 1$, the equality still holds. Note the summations span the entire grid by either summing over primal mesh cells i or by summing over edges e. The $\widehat{\cdot}$ operator averages a field from i to e or from e to i depending on the scalar in question: $\widehat{g_e}$ averages g_e to primal mesh cells, while $\widehat{h_i}$ averages h_i to edges. This identity is necessary in order to determine the proper discrete form of the kinetic energy, K_i, in Section 3.7.2.

We define averaging operators as:

$$(\widehat{g_e})_i = \frac{1}{A_i} \sum_{e \in EC(i)} g_e A_e / 4 \tag{A.9}$$

$$(\widehat{h_i})_e = \sum_{i \in CE(e)} h_i / 2. \tag{A.10}$$

Substituting (A.9) and (A.10) into (A.8) we find

$$\sum_i h_i \sum_{e \in EC(i)} g_e A_e / 4 = \sum_e g_e \frac{A_e}{2} \sum_{i \in CE(e)} h_i / 2. \tag{A.11}$$

As above, we demonstrate that (A.11) is true by showing that it holds at every edge. Without loss of generality, assume that for edge $e = 1$ that $i \in CE(e = 1)$ is composed of indices $i = 1$ and $i = 2$ as shown in Fig. 3. Evaluating (A.11) and retaining only those terms that couple $e = 1$ to $i = 1$ or $e = 1$ to $i = 2$ we have

$$h_1^{(i)} g_1^{(e)} A_1^{(e)} / 4 + h_2^{(i)} g_1^{(e)} A_1^{(e)} / 4 = g_1^{(e)} A_1^{(e)} (h_1^{(i)} + h_2^{(i)}) / 4 \tag{A.12}$$

which is true. So we can state that (A.8) holds as long was use (A.9) and (A.10) as the operators to average scalars from edges to cells and from cells to edges, respectively. We also note from (A.9) that the order of summation commutes, in that

$$\sum_i h_i \sum_{e \in EC(i)} g_e = \sum_e g_e \sum_{i \in CE(e)} h_i. \tag{A.13}$$

A.3. $\nabla \times \nabla h = 0$ identity

In order to prove this identity for arbitrary loops, the nomenclature needs to be broadened slightly by the definition of two sets. First let set N contain the integer indices of the nearest primal mesh neighbors to the primal grid cell i. In addition, let the set L contain an *ordered* list of length K of primal mesh cell indices where

$$L(k) \in N(i) \quad \text{and} \quad L(K) = L(1). \tag{A.14}$$

Eq. (A.14) forms a linked list of primal cells to create a discrete loop. In addition, we assume without loss of generality that $L(k)$ forms a single loop and is ordered in such a way as to produce a counter-clockwise (CCW) rotation with increasing k. The topology of the grid is assumed to be such that when traversing from k to $k+1$ a single edge e is crossed. These edges are essentially interleaved with the cells; two neighboring primal mesh cell indices are always associated with a single edge e and vice versa. Within this section let the edge residing between $L(k)$ and $L(k+1)$ be referenced as $e(k)$.

The intent is to determine a discrete analog to the weak form of $\nabla \times \nabla h = 0$,

$$\nabla \times \nabla h \approx \frac{1}{A_L} \sum_{k=1}^{K-1} \mathbf{G}_h(e(k)) \cdot \mathbf{d}_{e(k)}, \tag{A.15}$$

where $\mathbf{d}_{e(k)} = d_{e(k)}\,\mathbf{n}_{e(k)}$ and $e(k)$ is the unique edge interleaved between $L(k)$ and $L(k+1)$. Eq. (A.15) is consistent with the way that we define the curl operator in (23). The distance d_e has a magnitude of $|\mathbf{x}_{i+1} - \mathbf{x}_i|$ and is assumed here to point in the CCW direction around loop L. A_L is the area spanned by the entire loop. Using the discrete form of the gradient operator shown in (22), we find

$$\mathbf{G}_h(e(k)) = -\left[\frac{h(L(k+1))\,n_{e,L(k+1)} + h(L(k))\,n_{e,L(k)}}{d_{e(k)}}\,\mathbf{n}_{e(k)}\right]. \tag{A.16}$$

Substituting (A.16) into (A.15) results in

$$\nabla \times \nabla h \approx \frac{1}{A_L}\sum_{k=1}^{K-1}[h(L(k+1)) - h(L(k))]. \tag{A.17}$$

Since we have constrained L to be a single, closed, counter-clockwise loop, we are guaranteed that each $L(k)$ cell appears once and only once in the set L. Furthermore, during the summation in (A.17) over loop L, each cell appears exactly twice, once on the "front" end of gradient operator as $L(k+1)$ and once on the "back" end of the gradient operator as $L(k)$. Eq. (A.17) can be shown to sum to zero as

$$\nabla \times \nabla h \approx \frac{1}{A_L}\left[\sum_{k=1}^{K-1} h(L(k+1)) - \sum_{k=1}^{K-1} h(L(k))\right] \tag{A.18}$$

$$= \frac{1}{A_L}\left[\sum_{j=2}^{K} h(L(j)) - \sum_{j=1}^{K-1} h(L(j))\right] = 0. \tag{A.19}$$

The discrete curl of the discrete gradient sums identically to zero for any loop L that meets that criteria listed above.

References

[1] A. Adcroft, J. Campin, C. Hill, J. Marshall, Implementation of an atmosphere–ocean general circulation model on the expanded spherical cube, Monthly Weather Review (2004).
[2] A. Arakawa, V. Lamb, A potential enstrophy and energy conserving scheme for the shallow water equations, Monthly Weather Review (1981).
[3] A. Arakawa, Y.J.G. Hsu, Energy conserving and potential-enstrophy dissipating schemes for the shallow-water equations, Monthly Weather Review, 118(10) (1960, 1969) 1981.
[4] A. Arakawa, V.R. Lamb, Computational design of the basic dynamical processes in the ucla general circulation model, Methods in Computational Physics 17 (1977) 173–265.
[5] F. Aurenhammer, Voronoi diagrams – A survey of a fundamental geometric data structure, ACM Computing Surveys 23 (245) (1991) 405.
[6] L. Bonaventura, T. Ringler, Analysis of discrete shallow-water models on geodesic Delaunay grids with c-type staggering, Monthly Weather Review (2005).
[7] F.P. Bretherton, Critical layer instability in baroclinic flows, Quarterly Journal of the Royal Meteorological Society 92 (393) (1966).
[8] J. Cote, A Lagrange multiplier approach for the metric terms of semi-Lagrangian models on the sphere, Quarterly Journal of the Royal Meteorological Society 114 (483) (1988).
[9] Q. Du, V. Faber, M. Gunzburger, Centroidal voronoi tessellations: applications and algorithms, SIAM Review 41 (4) (1999) 637–676.
[10] Q. Du, M.D. Gunzburger, L. Ju, Constrained centroidal voronoi tessellations for surfaces, SIAM Journal on Scientific Computing 24 (5) (2003) 488–1506.
[11] Q. Du, M. Gunzburger, L. Ju, Voronoi-based finite volume methods, optimal voronoi meshes, and pdes on the sphere, Computer Methods in Applied Mechanics and Engineering 192 (35–36) (2003) 3933–3957.
[12] D.A. Ham, S.C. Kramer, G.S. Stelling, J. Pietrzak, The symmetry and stability of unstructured mesh C-grid shallow water models under the influence of Coriolis, Ocean Modelling 16 (1–2) (2007).
[13] R. Heikes, D. Randall, Numerical integration of the shallow-water equations on a twisted icosahedral grid. Part i: Basic design and results of tests, Monthly Weather Review 123 (1995) 1862–1880.
[14] B.J. Hoskins, M.E. McIntyre, A.W. Robertson, On the use and significance of isentropic potential vorticity maps, Quarterly Journal of the Royal Meteorological Society 111 (466) (1985).
[15] O. Kleptsova, J. Pietrzak, G. Stelling, On the accurate and stable reconstruction of tangential velocities in C-grid ocean models, Ocean Modelling 28 (2009).
[16] S.J. Lin, R.B. Rood, An explicit flux-form semi-lagrangian shallow-water model on the sphere, Quarterly Journal of the Royal Meteorological Society 123 (544) (1997) 2477–2498.
[17] W. Lipscomb, T. Ringler, An incremental remapping transport scheme on a spherical geodesic grid, Monthly Weather Review (2005).
[18] J. Marshall, D. Olbers, H. Ross, D. Wolf-Gladrow, Potential vorticity constraints on the dynamics and hydrography of the southern ocean, Journal of Physical Oceanography 23 (3) (1993) 465–487.
[19] J. McWilliams, A note on a consistent quasigeostrophic model in a multiply connected domain, Dynamics of Atmospheres and Oceans 1 (5) (1977) 427–441.
[20] S. Ničković, M.B. Gavrilov, I.A. Tošić, Geostrophic adjustment on hexagonal grids, Monthly Weather Review 130 (3) (2002) 668–683.
[21] R.A. Nicolaides, Direct discretization of planar div–curl problems, SIAM Journal on Numerical Analysis (1992) 32–56.
[22] R.L. Panton, Incompressible Flow, John Wiley & Sons, Inc., New York, 1996. pp. 1–840.
[23] B. Perot, Conservation properties of unstructured staggered mesh schemes, Journal of Computational Physics 159 (1) (2000) 58–89.
[24] T.D. Ringler, R. Heikes, D. Randall, Modeling the atmospheric general circulation using a spherical geodesic grid: a new class of dynamical cores, Monthly Weather Review 128 (7) (2000) 2471–2490.
[25] T.D. Ringler, D.A. Randall, A potential enstrophy and energy conserving numerical scheme for solution of the shallow-water equations on a geodesic grid, Monthly Weather Review 130 (5) (2002) 1397–1410.
[26] R. Sadourny, The dynamics of finite-difference models of the shallow-water equations, Journal of the Atmospheric Sciences 32 (4) (1975) 680–689.
[27] R. Sadourny, C. Basdevant, Parameterization of subgrid scale barotropic and baroclinic eddies in quasi-geostrophic models: anticipated potential vorticity method, Journal of the Atmospheric Sciences 42 (13) (1985) 1353–1363.
[28] W. Skamarock, A linear analysis of the ncar ccsm finite-volume dynamical core, Monthly Weather Review, January 2008.
[29] R.D. Smith, S. Kortas, Curvilinear coordinates for global ocean models, Los Alamos National Laboratory Technical Report, LA-UR-95-1146, 1995.

[30] G.R. Stuhne, W.R. Peltier, A robust unstructured grid discretization for 3-dimensional hydrostatic flows in spherical geometry: a new numerical structure for ocean general circulation modeling, Journal of Computational Physics 213 (2) (2006).
[31] P. Swarztrauber, Spectral transform methods for solving the shallow water equations on the sphere, Monthly Weather Review 124 (1996) 730–744.
[32] J. Thuburn, Multidimensional flux-limited advection schemes, Journal of Computational Physics 123 (1) (1996) 74–83.
[33] J. Thuburn, A pv-based shallow-water model on a hexagonal–icosahedral grid, Monthly Weather Review 125 (9) (1997) 2328–2347.
[34] J. Thuburn, Some conservation issues for the dynamical cores of nwp and climate models, Journal of Computational Physics 227 (7) (2008) 3715–3730.
[35] J. Thuburn, T. Ringler, J. Klemp, W. Skamarock, Numerical representation of geostrophic modes on arbitrarily structured C-grids, Journal of Computational Physics 228 (2009) 8321–8335.
[36] H. Tomita, M. Tsugawa, M. Satoh, K. Goto, Shallow water model on a modified icosahedral geodesic grid by using spring dynamics, Journal of Computational Physics (2001).
[37] Williamson, J. Drake, J. Hack, R. Jakob, P. Swarztrauber, A standard test set for numerical approximations to the shallow water equations in spherical geometry, Journal of Computational Physics 102 (1992) 211–224.
[38] S.T. Zalesak, Fully multidimensional flux-corrected transport algorithms for fluids, Journal of Computational Physics 31 (3) (1979) 335–362.